Applied Energy 281 (2021) 116115

Contents lists available at ScienceDirect

Applied Energy

journal homepage: www.elsevier.com/locate/apenergy

High-fidelity simulations and field measurements for characterizing wind fields in a utility-scale wind farm

Xiaolei Yang [a,b], Christopher Milliren [c], Matt Kistner [d], Christopher Hogg [e], Jeff Marr [c], Lian Shen [c,f], Fotis Sotiropoulos [g,*]

[a] The State Key Laboratory of Nonlinear Mechanics (LNM), Institute of Mechanics, Chinese Academy of Sciences, Beijing 100190, China
[b] School of Engineering Sciences, University of Chinese Academy of Sciences, Beijing 100049, China
[c] Saint Anthony Falls Laboratory, University of Minnesota, Minneapolis, MN 55414, United States
[d] Barr Engineering, Minneapolis, MN 55435, United States
[e] Xcel Energy, Minneapolis, MN 55401, United States
[f] Department of Mechanical Engineering, University of Minnesota, Minneapolis, MN 55455, United States
[g] Department of Civil Engineering, College of Engineering and Applied Sciences, Stony Brook University, Stony Brook, NY 11794, United States

ARTICLE INFO

Keywords:
Wind farms
Wind characterization
Large-eddy simulation
Field measurements

ABSTRACT

Characterizing wind farm flow fields at high temporal and spatial resolutions is critical prerequisite for the optimal design and operation of utility-scale wind farms and for reducing the levelized cost of energy. However, due to the large disparity of underlying scales, measurements or simulations alone cannot provide high resolution wind fields, which are informed by and account for the effect of both large scale (i.e. hour, day, month and year) and small scale (i.e. second and minute) site-specific variations in the atmosphere. We explore the feasibility of integrating field measurements and high-fidelity large-eddy simulation (LES) to characterize the wind field in a utility-scale wind farm while accounting for flow phenomena across multiple temporal scales. Specifically, we employ field measurements to characterize the monthly wind speed and wind direction distributions and investigate the wind characteristics in turbine wakes. It was found that the probability density function (PDF) of the wind speed in turbine wakes can be reasonably represented using the Weibull distribution but with shape factors smaller than those not in the wake. LES of the wind farm under statistically steady inflow is subsequently carried out for one wind direction. The LES predictions are compared with the measured data conditionally averaged based on the wind speed, wind direction and the root-mean-square of wind speed fluctuations over time intervals of 30 min. Good agreement is obtained for both mean wind speed and turbulence intensity. The present work shows the possibility of integrating field measurements and high-fidelity simulations for improved characterization of the site-specific wind fields in utility-scale wind farms.

1. Introduction

It is anticipated that wind will account for one-quarter to one-third of electricity supply across the world by 2050 based on the wind energy outlook by IEA [1], the energy transition outlook by DNV [2], and the new energy outlook by BNEF [3]. Characterizing the atmospheric turbulent flows in wind power plants [4] will be essential to the next generation wind technologies for even larger wind turbines and advanced turbine control at farm level [5]. In current practice, wind resource assessment can only give the mean wind speed distribution at very coarse grids and the annual distributions of wind speed and wind directions, which are then employed together with the engineering models for turbine wakes for the layout design of wind farms [6–8]. Such approaches cannot properly incorporate the spatially heterogeneous wind distribution or take into account turbine wake interactions in the design process. Consequently, the power production from the designed wind farm could be lower than expected, while the fatigue loads on turbine structures may be significantly higher. To design wind farms with high power output and low maintenance cost requires not only time-averaged wind speed data at several meteorological tower locations but also field data at a high spatial resolution, which cannot be easily obtained from field measurements [9,10] or mesoscale simulations [11,12]. On the other hand, high-fidelity simulations can predict wind field at high spatial and temporal resolutions but often for a short time interval limited to hours or even less. Combining

* Corresponding author.
E-mail address: fotis.sotiropoulos@stonybrook.edu (F. Sotiropoulos).

https://doi.org/10.1016/j.apenergy.2020.116115
Received 24 June 2020; Received in revised form 20 October 2020; Accepted 23 October 2020
Available online 27 October 2020

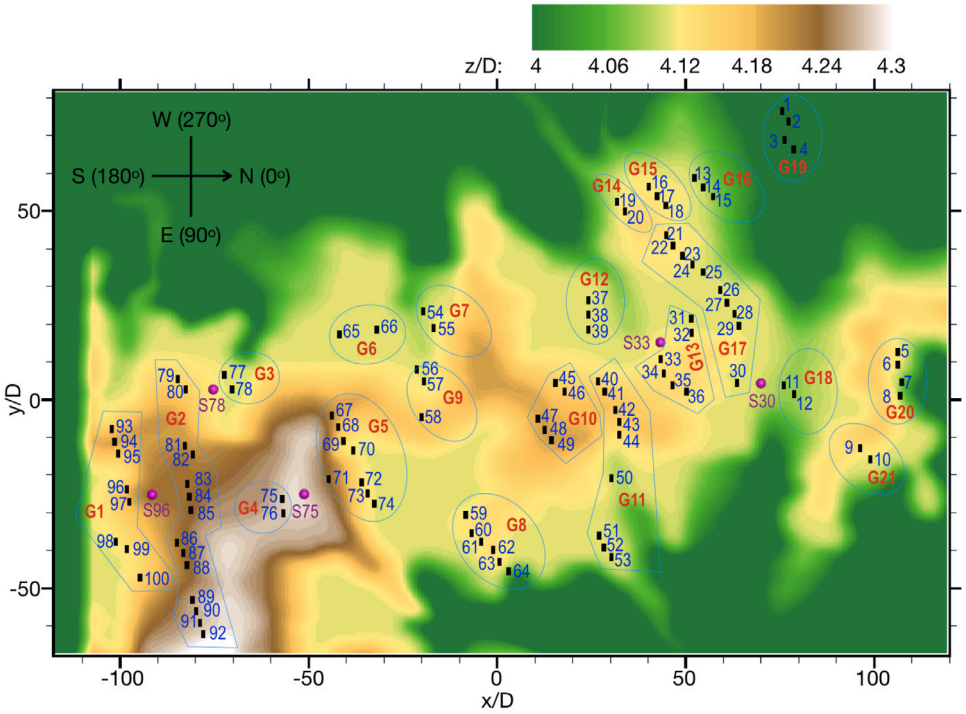

Fig. 1. Contours of terrain elevation with black line segments for turbine locations and purple points for SODAR locations. Positive x axis aligns with the north direction.

Table 1
Dates for data collection in the wind farm located in Pleasant Valley, Minnesota, United States in 2017.

S30	S33	S75	S78	S96
05/03–06/05	06/07–07/10	07/12–08/14	08/16–09/18	09/19–10/26

the power of field measurements and high-fidelity simulations has the potential to characterize the wind field at high spatial and temporal resolutions and for a long time interval, which will enable realizing significant increases in annual energy production and reductions in the levelized cost of energy. We propose integrating field measurements and high-fidelity simulations results for characterizing turbulent flows in utility-scale wind farms. As the first step towards this direction, in this work we employ field measurements to study the wind speed distribution in turbine wakes and examine the predictive capability of a 30-minutes high-fidelity simulation by comparing the computed results with conditionally-averaged wind data measured over months.

Wind resource assessment methods include global reanalysis datasets, measurements, mesoscale modeling, combined meso/microscale modeling and others as reviewed by Landberg [13]. Other reviews on wind resource assessment techniques can be found in other literatures for [14] focusing on computational models, [15] focusing on offshore wind resource assessment and [16] for the trends in wind resource assessment, respectively. The coarse resolution global reanalysis is often employed for global or large-scale regional wind resource analysis. For instance, Christiansen et al. [17] constructed wind maps using satellite synthetic aperture radar (SAR) data and validated the results against in situ measurements from an offshore mast in the North Sea. He and Kammen [18] employed GIS modeling utilizing 10 years of hourly wind speed data at 200 representative locations to assess provincial wind resources in China. The global reanalysis is also integrated with other approaches for detailed resource assessment. For instance, Doubrawa et al. [19] employed satellite wind data, in-situ measurements at coastal stations and buoys, and WAsP (Wind Atlas Analysis and Application Program) to obtain the wind climate map at Great Lakes. Using the global wind data as boundary conditions, mesoscale simulations can be employed for wind resource assessments of potential sites in a region. For instance, Acker [20] employed a mesoscale numerical weather prediction (NWP) model and 30-years historical data for wind resource assessment in the state of Arizona, United States. Jafari et al. [21] examined the effects of horizontal spatial resolutions when using NWP models for wind resource assessments. Al-Yahyai [22] reviewed the use of NWP models for wind resource assessments and stated the advantages of using NWP models as compared with measurements, e.g. cost, spatial resolutions and others. Mesoscale simulations are often coupled with microscale simulations for detailed wind resource assessment. Carvalho et al. [23] evaluated three different approaches for coupling the mesoscale simulations using Weather Research and Forecasting model (WRF) with the microscale simulations using WAsP. Gasset et al. [24] compared various models for coupled mesoscale/microscale simulations by comparing simulated mean wind speeds with measurements, and showed improved results by resolving more topography features of the terrain. Defforge [25] employed the iterative ensemble Kalman smoother to assimilate the observation data to improve the accuracy of boundary conditions in local scale simulations, which are often obtained from mesoscale simulations and affect the reliability of simulations at local scale. Veronesi et al. [26] employed an approach based on regression trees to estimate wind speed and direction distributions over the United Kingdom.

Wind field characteristics at farm scale are often obtained using WAsP simulations or Reynolds-Averaged Navier–Stokes (RANS) simulations together with measurements. For instance, Aukitino et al. [28] carried out the wind resources assessment of Kiribati using measurements at two locations and WAsP. Palma et al. [29] employed WAsP and RANS model for wind resource assessment in complex terrain. Jimenez et al. [30] found that the accuracy of the WAsP predictions depends on the measurement station used for reference. Yan and Li [31] employed RANS simulations and measurements using the cup anemometer at one location to assess the wind resource of a complex terrain site in Hong Kong, China. Tang et al. [32] employed RANS simulations with corrections based on measurements at several masts to characterize wind resource in complex terrain. Song et al. [33] developed an anemometer graph approach using the observations at a single

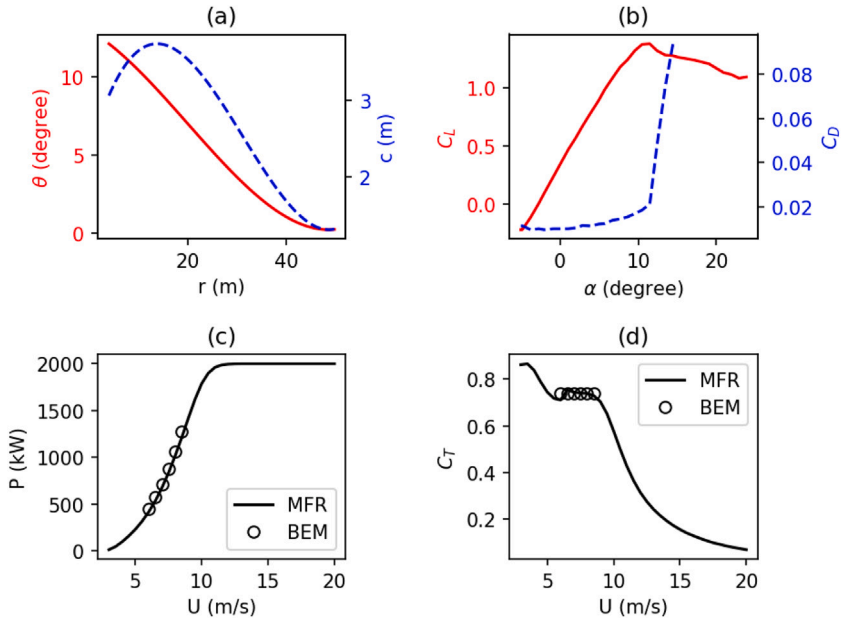

Fig. 2. The employed turbine design for (a) radial distributions of twist angle and chord of the blade, (b) lift and drag coefficients of the employed airfoil FFA-W3 [27], (c) power curve and (d) thrust coefficient. In (c) and (d), MFR for P or C_T curve from the wind turbine manufacturer and BEM for results from blade element momentum method.

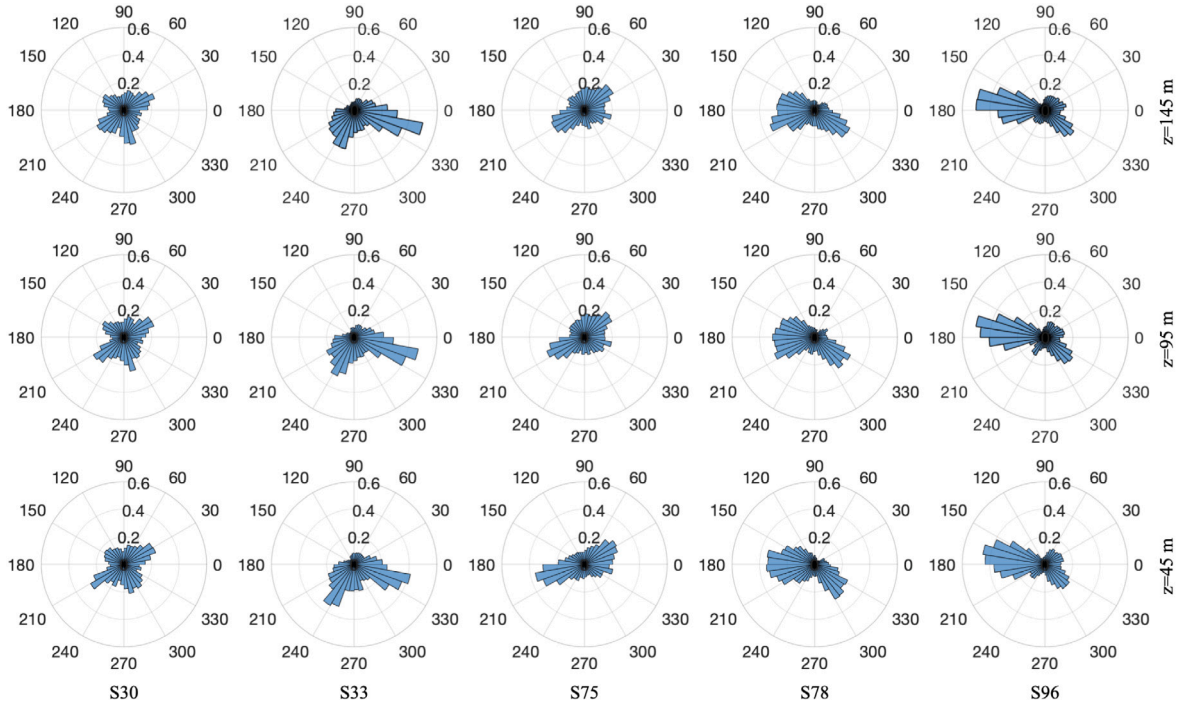

Fig. 3. PDF of wind direction at $z = 45$ m, $z = 95$ m and $z = 145$ m above the ground for all wind speeds at different SODAR locations. The figure shows the angle in degrees. It is noticed that the PDF is calculated based on radians instead of degrees.

anemometer to find the proper velocity conditions at the inlet for RANS simulations for wind resource assessment in complex terrain. Simões and Estanqueiro employed RANS [34] for wind resource assessment in urban areas. A measure-correlate-predict (MCP) approach is often employed for long-term wind resource assessments based on measurements or simulations at the selected site and the long-term dataset at the reference site. For instance, Bechrakis et al. [35] employed the artificial neuron network to obtain annual wind resource by relating the short term measurements at the site of concern with the one year wind data at another reference site. Weekes and Tomlin [36] compared MCP approaches based on different regression techniques for long-term wind resource using three months measurements. Vanvyve [37] developed an ensemble analog approach for long-term wind speed estimations using the short-term observation record from the target site and the long-term historical data from a nearby site. Sharma et al. [38] employed LiDAR (light detection and ranging) and MCP method for offshore wind resource assessment. Lackner et al. [39] carried out uncertainty analysis for MCP based wind resource assessment, which includes the wind speed measurement uncertainty and the uncertainty in the parameter for the Weibull distribution. Miguel et al. [40] found

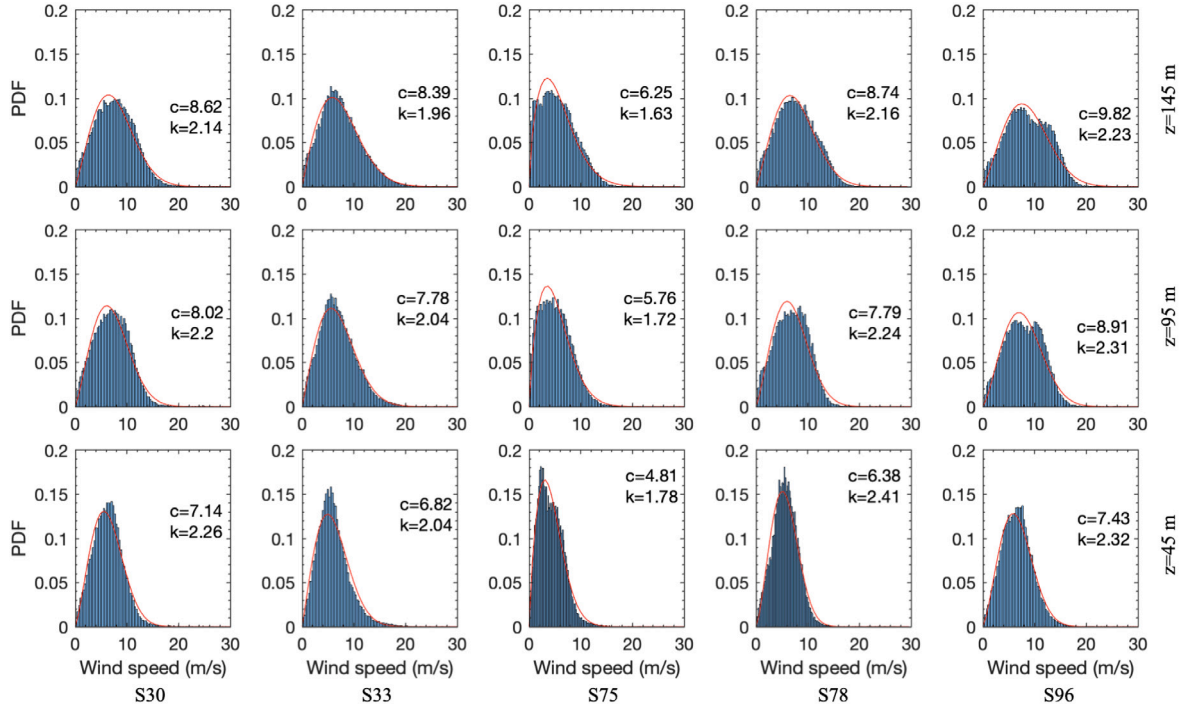

Fig. 4. PDF of wind speed at $z = 45$ m, $z = 95$ m and $z = 145$ m above the ground for all wind directions at different SODAR locations. The red solid lines show the best-fitted Weibull distributions.

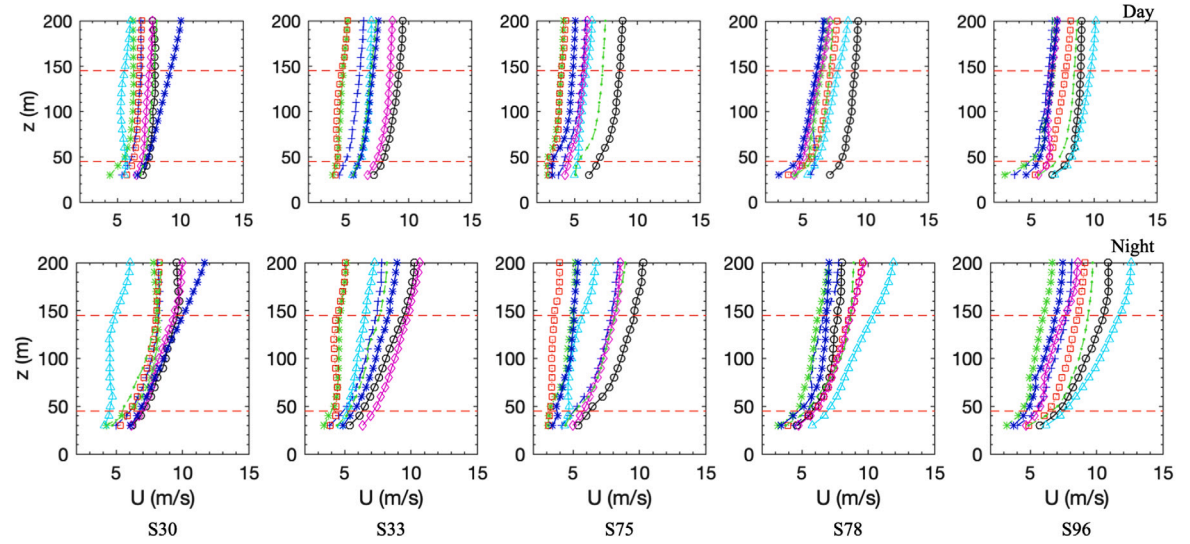

Fig. 5. Vertical profiles of mean wind speed for different wind directions at different SODAR locations. Black solid line with circles: 0° ± 22.5°; Blue-dashed line with crosses: 45° ± 22.5°; Green dash–dot line with asterisks: 90° ± 22.5°; Red dotted line with squares: 135° ± 22.5°; Cyan solid line with triangles: 180° ± 22.5°; Magenta solid line with diamonds: 225° ± 22.5°; Blue solid line with asterisks: 270° ± 22.5°; Green dashed line with points: 315° ± 22.5°.

that the level of uncertainty decreases by increasing the duration of data collection campaign.

We can summarize that there are two major limitations in the current approaches for wind resource characterizations, i.e. (1) cannot properly consider the effects of turbine wakes, and (2) cannot accurately predict velocity fluctuations due to atmospheric turbulence. To address these issues, in this work we propose to integrate field measurements and large-eddy simulation (LES) for characterizing wind fields at farm scale. Considering wake effects in wind farm design requires knowledge of the wind speed distribution in turbine wakes. The annual distributions of wind speeds and wind directions are often characterized using the Weibull distribution as follows,

$$p(U)dU = \frac{k}{c}\left(\frac{U}{c}\right)^{k-1}\exp\left[-\left(\frac{U}{c}\right)^{k}\right]dU \tag{1}$$

where k is the shape factor (dimensionless), c is the scale factor (m/s) related to the annual mean wind speed $\overline{U}$ by the relationship, $c = \overline{U}/\Gamma(1+1/k)$, where Γ is the complete gamma function. In the literature the value of the shape factor k is around 2 without considering specific locations or wind directions [41,42]. Veronesi et al. [26] studied the spatial distributions of the shape factor and the scale factor over the United Kingdom based on the measured data and the random forest method. Whether the Weibull distribution is a proper choice for the wind speed in turbine wakes is not clear and cannot be verified using

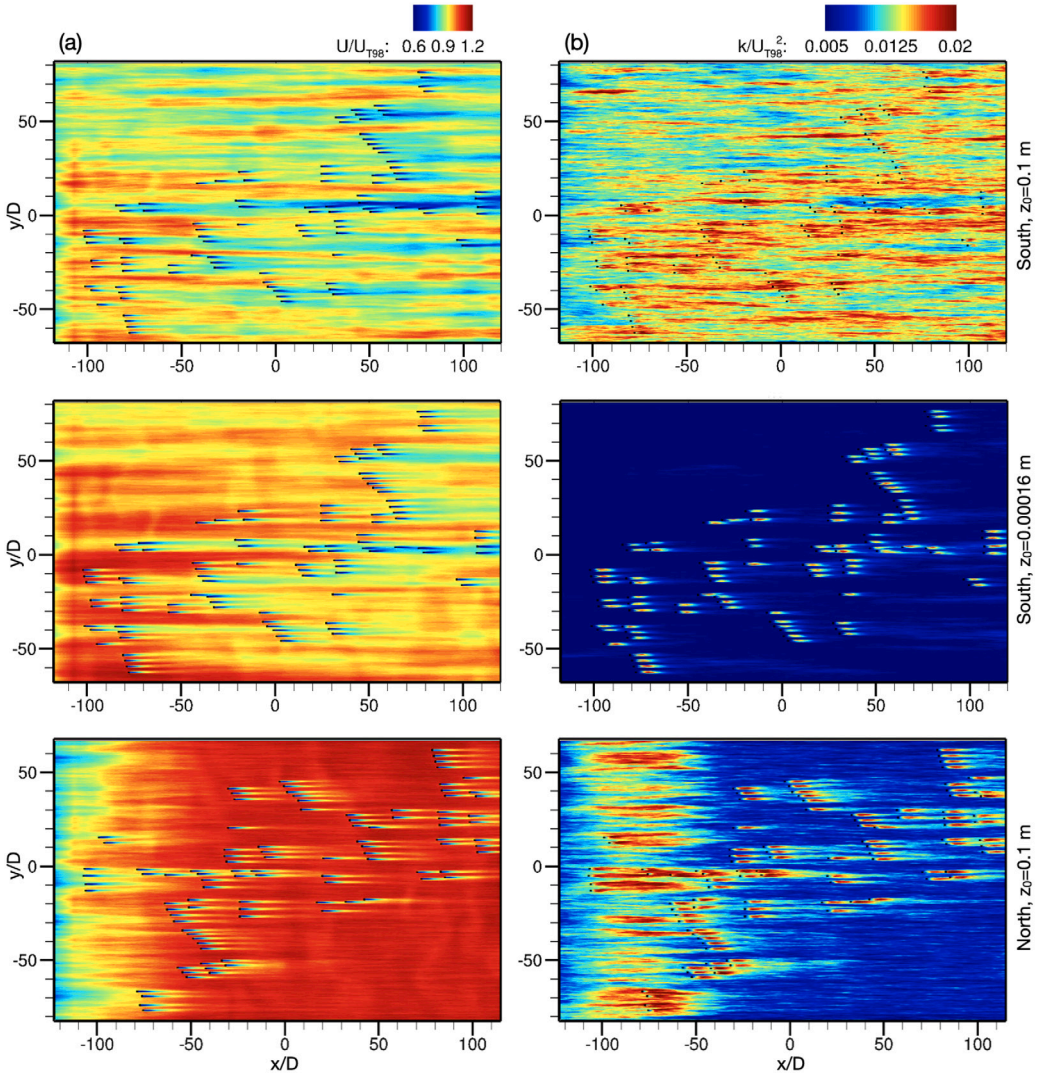

Fig. 6. Contours of the flowfield from LES for (a) time-averaged downwind velocity U and (b) turbulence kinetic energy k on a plane z_h from the ground for different cases.

high-fidelity simulation without taking into account daily or monthly variations of wind speeds, which, on the other hand, can be obtained from field measurements. In this work we employ the data measured using SODAR (SOnic Detection And Ranging), which can be placed in the wind farm without impacting its operation, to examine the wind speed distribution in turbine wakes.

Validation of high-fidelity LES models against field measurements is often carried out for a short time interval (minutes to hours) during which the wind does not change significantly. In such studies idealized inflow conditions (e.g. uniform inflow and statistically steady inflow) can be employed in LES. For instance, in [43] LES results under uniform inflow condition are compared with field data measured for wind speed in the range of 5–74 m/s. In [44] LES results of a wind farm were compared with measured data for an hour during which the atmospheric stability was near-neutral, and the magnitude and the direction of the wind were quasi-stationary. In [45], LES results of five turbines in a wind farm, simulated by prescribing inflow velocity field obtained from a mesoscale simulation and superimposing velocity fluctuations obtained using the synthetic turbulence method, are compared with the wind data measured over two hours when the wind of speed 11 m/s was from the south direction. In [46] LES results of a wind farm in complex terrain were compared with measurements for 30 min during which the wind direction was in the range of 280°–290° and the wind speed was about 9–11 m/s. To apply high-fidelity simulations to the design of a wind farm, it is important to limit the number of required simulations for design efficiency. This is possible, however, only if one simulation can be a representative of different wind conditions. Therefore, and the second objective of this work, we will examine herein how well simulation results from a high-fidelity simulation for a short time compare with data measured over months.

The rest of the paper is organized as follows. First, we describe numerical methods, computational setup and field measurements in Section 2. Then we present the measured and computed results, and propose a potential solution for integrating the measurements and simulations for the optimization of wind farm layout and operation in Section 3. Finally we draw the conclusions in Section 4.

2. Field site, numerical methods, and computational setup

2.1. Field site

The studied wind farm is located in Pleasant Valley, Minnesota, United Stated. The turbines installed are the Vestas V100-2.0 MW wind turbine of rotor diameter 100 meters and hub height 95 m. The cut-in, rated and cut-out wind speed are 3 m/s, 12 m/s and 20 m/s, respectively. Fig. 1 shows the contours of the terrain elevation of the studied site. It is seen that the range of terrain elevations is about $0.3D$, which is 30 m. In this figure, turbines are represented by black

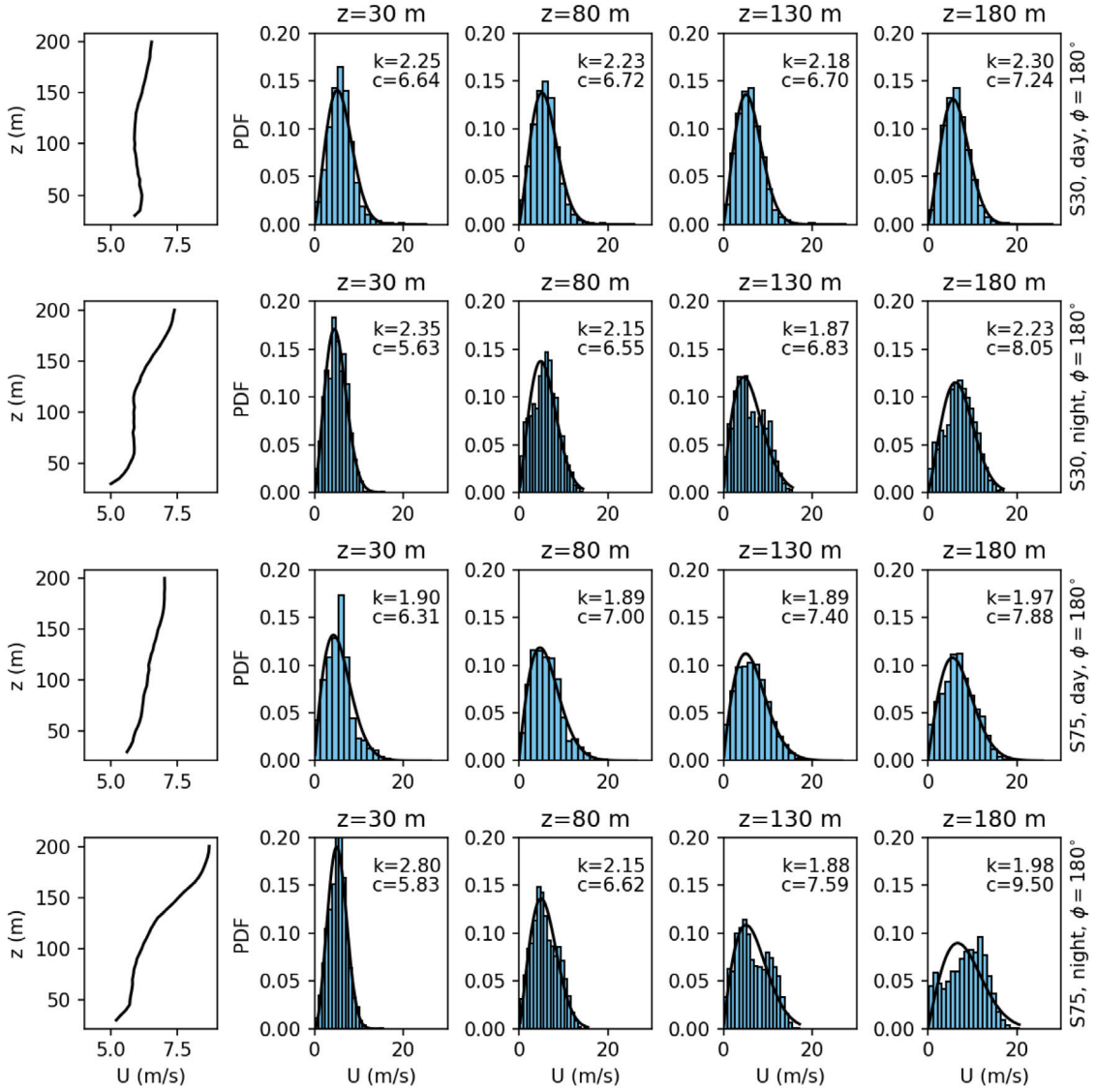

Fig. 7. PDF of wind speed fluctuations in a turbine's wake for different vertical locations. The measured data at S30 and S75 SODAR locations when the wind blows from the south direction ($180° \pm 22.5°$) are examined. The wind direction is determined using the one measured at $z = 200$ m. The vertical profiles of the corresponding wind speed are shown in the far left column. The solid lines are the best-fitted Weibull distributions.

line segments. It is seen that the turbines are mostly positioned along the ridges of the terrain. The five SODAR measurement locations are denoted by purple dots. In the simulations with the VFS-Wind code we only consider the case when wind blows from the south direction (negative x in Fig. 1). To facilitate the comparison between simulations and SODAR measurements the turbines are divided into 21 groups based on their relative locations. The data collection campaign for this study in this wind farm was conducted from March 17, 2017 to October 26, 2017. SODAR was employed for measuring the wind speed and wind direction at five different locations in the wind farm. The wind data collected from $z = 30$ m to $z = 200$ m at increment of 5 meters for every minute will be analyzed in this work. As shown in Fig. 1 the five SODAR locations S30, S33, S75, S78 and S96 are close to five wind turbines named as T30, T33, T75, T78 and T96, respectively. The measurement was taken for about a month at each SODAR location as listed in Table 1.

2.2. Numerical methods

The high-fidelity Virtual Flow Simulator (VFS-Wind) code [45,47] is employed for simulating the atmospheric turbulent flow over the wind farm. The governing equations are the spatially filtered continuity equation and the incompressible Navier–Stokes equation in non-orthogonal, generalized, curvilinear coordinates ξ^i, which read in compact tensor notation (repeated indices imply summation) as follows $(i, j = 1, 2, 3)$:

$$J\frac{\partial U^j}{\partial \xi^j} = 0, \tag{2}$$

$$\frac{1}{J}\frac{\partial U^i}{\partial t} = \frac{\xi_l^i}{J}\left(-\frac{\partial (U^j u_l)}{\partial \xi^j} + \frac{\mu}{\rho}\frac{\partial}{\partial \xi^j}\left(\frac{g^{jk}}{J}\frac{\partial u_l}{\partial \xi^k}\right) - \frac{1}{\rho}\frac{\partial}{\partial \xi^j}\left(\frac{\xi_l^j p}{J}\right) - \frac{1}{\rho}\frac{\partial \tau_{lj}}{\partial \xi^j} + \frac{1}{\rho}f_l\right), \tag{3}$$

where $\xi_l^i = \partial \xi^i / \partial x_l$ ($(x_i$ (i = 1, 2, 3) for Cartesian coordinates)) are the transformation metrics, J is the Jacobian of the geometric transformation, u_i is the ith component of the velocity vector in Cartesian coordinates, $U^i = (\xi_m^i / J)u_m$ is the contravariant volume flux, $g^{jk} = \xi_l^j \xi_l^k$ are the components of the contravariant metric tensor, ρ is the density, μ is the dynamic viscosity, α is the thermal diffusivity, p is the pressure, $f_l (l = 1, 2, 3)$ are the body forces introduced by the wind turbines, and τ_{ij} represents the anisotropic part of the subgrid scale stress tensor, which is modeled by the dynamic eddy-viscosity subgrid scale model [48]. Second-order central differencing is employed for

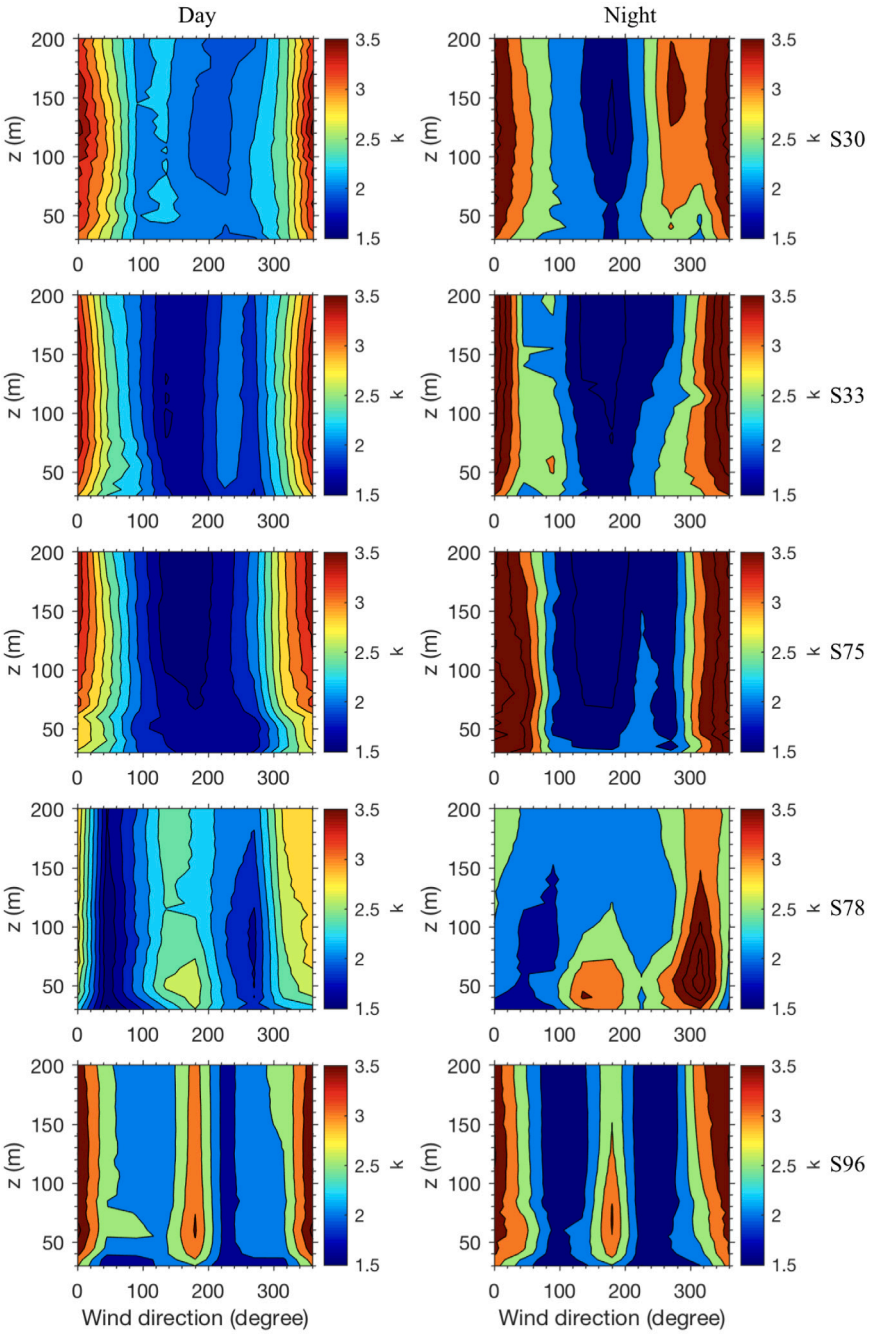

Fig. 8. Contours of the shape factor k for the best-fitted Weibull distribution at different SODAR locations for days (left column) and nights (right column).

spatial discretization. A second-order accurate fractional step method is used for advancing the continuity and momentum equations. An algebraic multigrid acceleration along with GMRES (Generalized minimal residual method) solver is used to solve the pressure Poisson equation and the matrix-free Newton–Krylov method is used for solving the momentum equation. The VFS-Wind code has been validated extensively using laboratory and field measurements [45,47,49,50] and applied to utility-scale wind turbines [51–54].

In this work, an actuator line model [45] is employed for parameterizing the effect of turbine blades. In the employed actuator line model, the rotor blade is represented using a rotating line with distributed forces to model the interaction between the rotating blades and the incoming wind. The force on the actuator line is a function of geometry (e.g. twist angle and chord length) and aerodynamic (e.g. lift and drag coefficients) characteristics of the blade, and is computed based on the blade element approach. The nacelle is modeled by simply extending the actuator line to the center of the rotor. The grid nodes discretizing the actuator line in general do not coincide with the background grid nodes employed for solving the flow. The discrete delta function is employed for distributing forces from the actuator line grid nodes to the surrounding background grid nodes, which can guarantee the conservation of force and torque during the force distribution [55]. Actuator surface models, which have also been proposed in the literature for both horizontal axis and vertical axis wind turbines [47,56,57], which generally require spatial resolution higher than actuator disk/line models, are not employed in this work.

2.3. Computational setup

Three cases have been carried out. In two of the three cases for wind from the south direction, we consider two different roughness lengths,

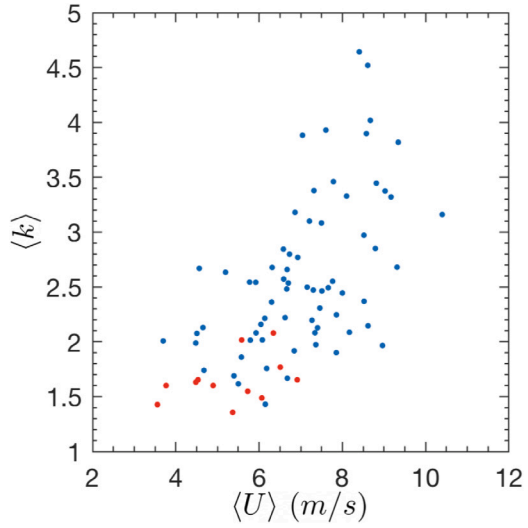

Fig. 9. Variations of the vertical averaged shape factor k as a function of vertical averaged wind speed, in which the data points are from eight evenly divided wind direction sectors for days and nights for all SODAR locations. The red points show the SODAR measurements in turbine wakes. (For interpretation of the references to color in this figure legend, the reader is referred to the web version of this article.)

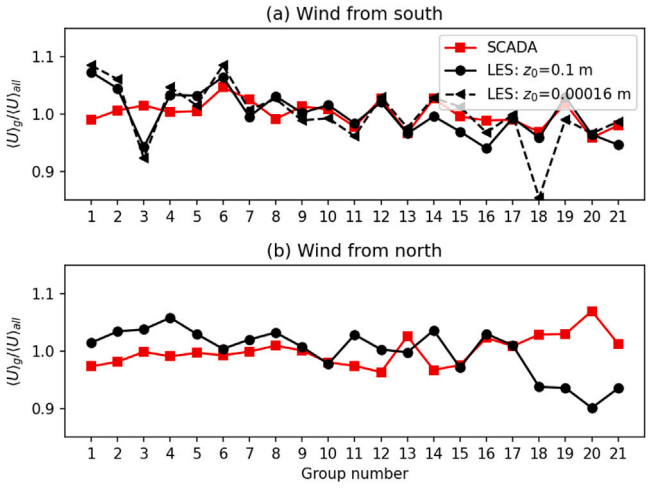

Fig. 10. Comparison of incoming wind speed between LES predictions (black lines with circles and triangles) and SCADA data (red solid lines with squares) for different groups of wind turbines for (a) wind from south and (b) wind from north, respectively. The SCADA data for wind direction in the ranges of $180° \pm 5°$ and $0° \pm 5°$ are employed in (a) and (b), respectively. The wind blows from small group number to large group number for (a) and vice versa for (b).

i.e. $z_0 = 0.00016$ m and 0.1 m, which are typical for calm open sea or snow-covered land [58,59] and surface covered by thick grass [59] representing two extreme surface conditions of the wind farm region. In the third case, the wind blows from the north direction with the surface roughness fixed at $z_0 = 0.1$ m. In the simulation, the terrain is represented using a terrain-fitted curvilinear grid. The computational domain is $L_x \times L_y = 240D \times 150D$ in the downwind and spanwise directions, respectively. In the vertical direction, the top boundary is a flat plane located at $10D$ from the ground measured in the region near the inlet, where the surface is set as flat as shown in Fig. 1. In other regions, the height of the computational domain is not necessarily $10D$ because of the elevation of the terrain. The number of grid nodes is $N_x \times N_y \times N_z = 1183 \times 1487 \times 61$ with the grid spacing of $\Delta x \approx D/5$, $\Delta y = D/10$ and $\Delta z = D/20$ in the downwind, spanwise and vertical (for $z < 2D$) directions, respectively. The mesh is evenly distributed in the horizontal directions. In the vertical direction, the mesh is uniform for $z < 2D$ and stretched upward to the top boundary. The size of the computational time step is $\Delta t = 0.01D/U_h$. The time and spanwise-averaged incoming wind speed at turbine hub height is $U_h \approx 8$ m/s from the south/north direction. The free slip boundary condition is applied at the top and spanwise boundaries. At the bottom boundary, a wall model is applied along with non-flux boundary condition and the wall shear stress τ_w computed from the logarithmic law for rough walls. The incoming turbulent flow is generated from a precursory simulation of flat terrain with periodic boundary conditions applied in the horizontal directions.

In this precursory simulation, the flow is driven by a mean pressure gradient obtained by maintaining a constant mass flux without considering the Coriolis force. The size of the employed computational domain is $L_x \times L_y \times L_z = 225D \times 150D \times 10D$ with number of grid nodes $N_x \times N_y \times N_z = 1126 \times 1487 \times 152$. The size of time step is $\Delta t = 0.1D/U_h$. The roughness length is $z_0 = 0.00016$ m. For the wind farm case with the same roughness length, the generated inflow is directly applied at the inlet of the computational domain. For the cases with $z_0 = 0.1$ m, we do not generate the inflow from another simulation with periodic boundary conditions in downwind direction. Instead we apply the inflow from the precursory simulation with $z_0 = 0.00016$ m to a simulation with inlet–outlet boundary condition in the downwind direction and surface roughness length of $z_0 = 0.1$ m, and employ the velocity field close to the outlet of this simulation as the inflow for the wind farm simulation. Other setups of this simulation are the same as the precursory simulation with $z_0 = 0.00016$ m. Streamwise development of the downwind velocity and turbulence kinetic energy for this precursory simulation with inlet–outlet boundary condition can be found in the appendix. It is noted that spatial and temporal interpolation is performed on the generated inflow to account for different grid spacings and sizes of time step employed in the precursory simulation and the wind farm simulation. To specify the inflow conditions, a flat plane bottom boundary is applied at the inlet of the computational domain starting at $x = -120D$ and extending up until approximately $x = -110D$ where the bottom boundary transitions to the natural terrain elevation. The atmospheric stability is set as neutral in the present cases because of the lack of temperature measurements (only available at one vertical position), which may not be correct especially for the time during nights. This introduces uncertainties to LES and may contribute to the discrepancies between the LES predictions and measurements. The wind farm simulation is first carried out until the total kinetic energy reaches a quasi-steady state, and subsequently the instantaneous flowfields are averaged for $100D/U_h$ time units (approximately 30 min of physical time) for computing the statistics of oncoming velocity for different turbines and the velocity at different locations.

The blade geometry information of the actual Vestas V100 wind turbine is not available. In this work, we employ the FFA-W3 airfoil for the entire blade, which was employed in [60] for the Vestas V80-2MW wind turbine. This is certainly not an optimal design of the blade considering many other constraints like the cost of the material and the strength of the structure, while is just to ensure the power production and thrust coefficient of the employed design the same as the actual Vestas V100 wind turbine. The radial distributions of the twist angle and chord of the blade (shown in Fig. 2(a)) are tweaked in a way that the rated power is 2 MW, i.e. the same as the installed wind turbine. The lift and drag coefficients of the airfoil FFA-W3-241 at $Re = 1.6\times10^6$ (as shown in Fig. 2(b)) are employed assuming the Reynolds number effect is negligible [61]. The power curve (P) and thrust coefficients (C_T) are shown in Fig. 2(c) and (d), respectively, in which the P and C_T computed from the blade element momentum method [62] are compared with those from the wind turbine manufacturer. As seen, the P and C_T of the employed wind turbine agree well with the actual Vestas V100 wind turbine. In this work, the power is computed using the rotor rotational speed and the aerodynamic torque on the rotor.

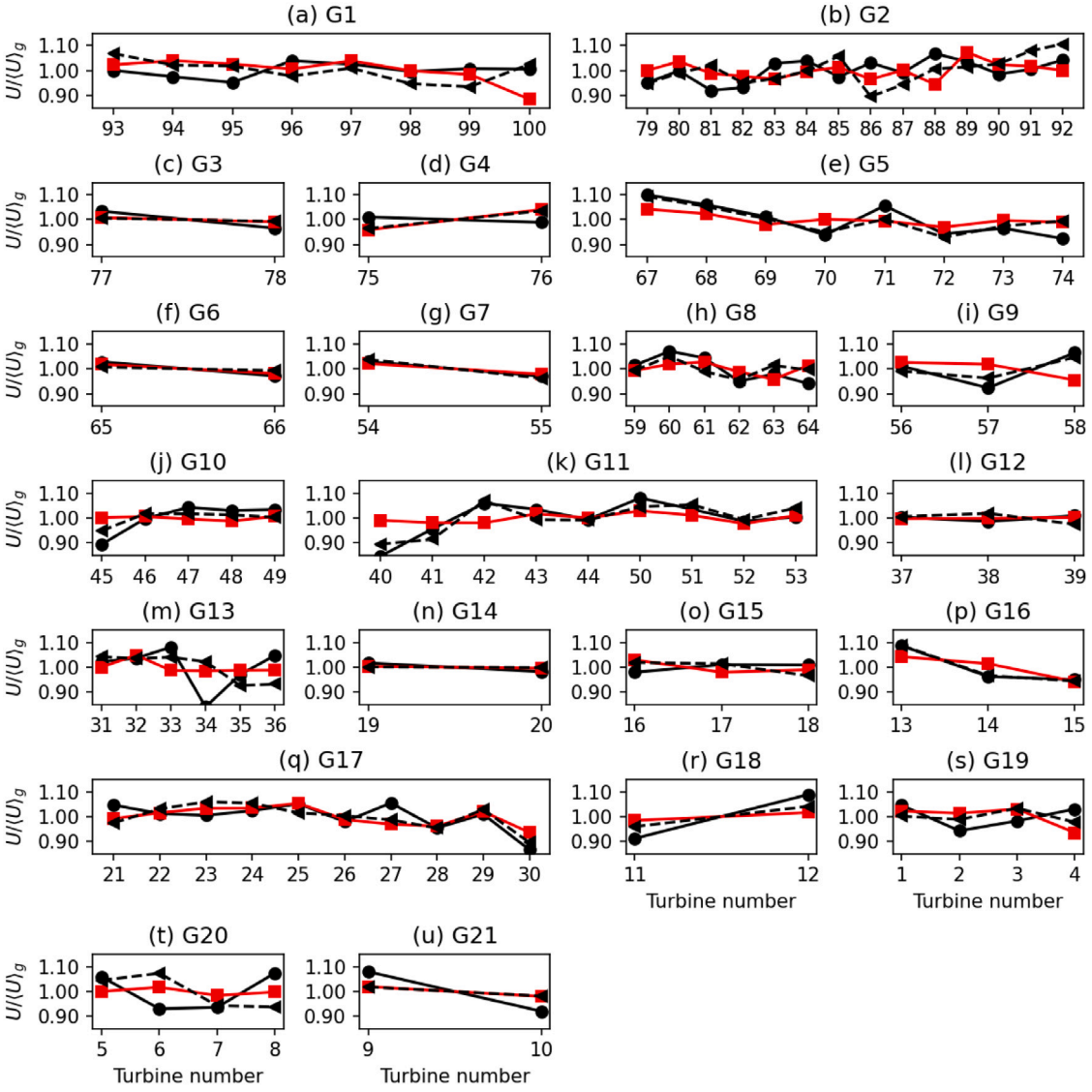

Fig. 11. Comparison of incoming wind speed between LES predictions (black solid lines with squares) and SCADA measurements (red solid lines with circles) for wind turbines in each group for the cases with wind from the south direction. The wind direction of the SCADA data is in the range of $180° \pm 5°$.

It is noted that we only compare P and C_T for a certain range of velocity, in which the rotor rotates at the optimal tip-speed ratio, i.e. $\lambda = \Omega R/U_\infty = 9$ (where λ is the tip-speed ratio, Ω is the rotor rotational speed, R is the rotor radius and U_∞ is the incoming wind speed), with blade pitch fixed at 1°. Outside this velocity range, the control system of the turbine, which is often not provided by the wind turbine manufacturer, needs to be inversely designed and calibrated based on the available information of the turbine (e.g. power curve and thrust coefficient) to give the relation between the rotor rotational speed and the aerodynamic torque.

3. Results

In this section we first show the wind speed and wind direction distributions from the SODAR measurements and the flowfield computed using LES for a general description of the wind in the studied wind farm. In Fig. 3 we examine the probability density function (PDF) of measured wind directions. As seen during the data collection campaign, the wind is roughly along the south–north direction, which is aligned with the predominant direction of the wind farm layout. During September and October (S96 measurements), the wind mainly blows from the south direction, which is the wind direction considered in the LES case. It should be noted that the LES data will be compared with measured data from all SODAR locations (see Table 1) when the wind blows from the south direction instead of only the data measured at S96 (see Fig. 1) as a main objective of this work is to examine what LES can predict for a certain wind direction rather than focusing on a specific period of time when the wind speed does not change a lot. The vertical variations of wind direction are also examined in Fig. 3. As seen, the wind direction distributions are very similar at the three considered vertical positions, although some differences are observed at S75 and S33, which are located at the top of the hill and deep in the farm, respectively, where the vertical distributions of wind directions can be significantly altered by the topography change and upwind turbine wakes. In Fig. 4 we examine the PDF of the measured wind speed for all wind directions, in which the bars are the measured data and the red lines are the Weibull distributions with coefficients best-fitted using the measured data. From this figure, it is seen that the PDFs of wind speed are well represented by the Weibull distribution for all SODAR locations corresponding to different months of the year, different terrain topography and different local turbine layouts. Different values of the scale factor c and shape factor k are observed for different SODAR locations. At the same location the shape factor is similar at $z = 45, 95$

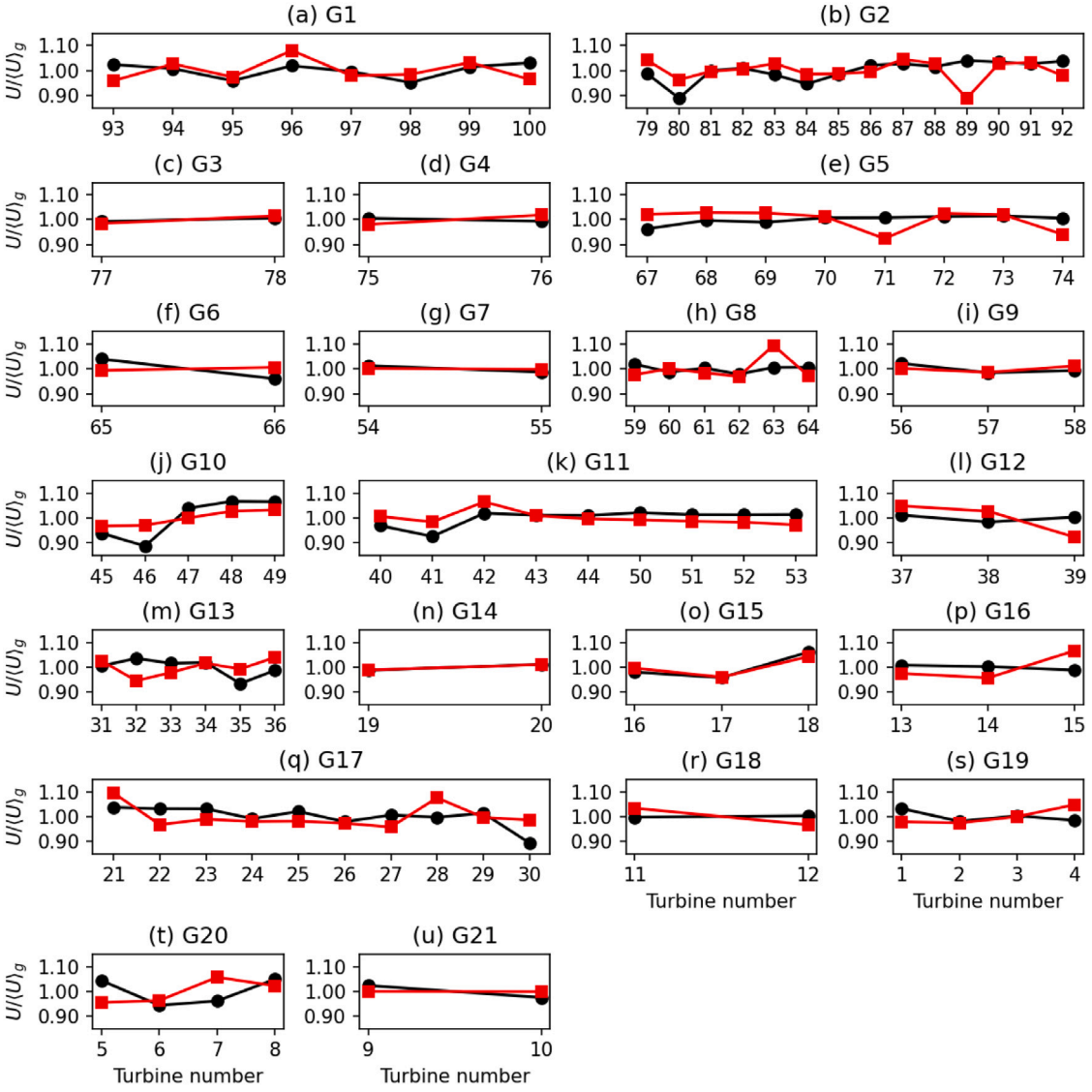

Fig. 12. Comparison of incoming wind speed between LES predictions (black solid lines with squares) and SCADA measurements (red solid lines with circles) for wind turbines in each group for the case with wind from the north direction. The wind direction of the SCADA data is in the range of $0° \pm 5°$.

and 135 m above the ground, while the scale factor, which depends on the time-averaged wind speed, is observed to increase with z from $z = 45$ m to 135 m. In Fig. 5 we examine the mean wind speed profiles at different SODAR locations, which are averaged using the wind data collected during days and nights based on 8 wind direction sectors, i.e. 0°±22.5°, 45°±22.5°, 90°±22.5°, 135°±22.5°, 180°±22.5°, 225°±22.5°, 270°±22.5° and 315°±22.5°. Because of the stable atmospheric condition the wind speed and the change of wind speed across the rotor plane are observed greater during nights for the same wind direction. Wake profiles are observed in Fig. 5 for certain wind directions at some SODAR locations, for instance, the wake of turbine T30 is observed at SODAR S30 location for wind from the south direction.

Field measurements can provide monthly and yearly wind variations at the selected site [63–68]. However, it is challenging to obtain wind data at the spatial resolution (~ m) needed to develop new generation wind turbine and farm control strategies over the entire wind farm (~ km) using field measurements. High-fidelity LES, on the other hand, can complement the wind characterization by providing the spatial distributions of wind speed and turbulence statistics [46,69–71]. Fig. 6 shows the time-averaged downwind velocity U and turbulence kinetic energy k on a plane located at the turbine hub height. It is observed that the distributions of U and k are different for cases with different wind directions. For the two cases with the same wind direction, the overall patterns of the downwind velocity are similar for different roughness lengths. For the case with wind from south and $z_0 = 0.1$ m, the level of turbulence kinetic energy in turbine wakes is similar to that in the environment, while is significantly higher compared with that in the environment for the case with z_0=0.00016 m. For the case with wind blowing from the north, it is seen that the normalized U is higher and distributed more uniformly in the wind farm region. Because of the increase of terrain elevation as wind blows from north to south, the level of turbulence kinetic energy is significantly reduced with the turbulence in turbine wakes prevailing in the wind farm region. Overall, the spatially non-homogeneous distributions of downwind velocity and turbulence kinetic energy are well captured by the LES, which are induced by the terrain topography and turbine wakes and are important for developing advanced turbine and farm control algorithms, such as yaw control and pitch control. On the other hand, the long-term wind variations in *turbine wakes*, e.g. for months, weeks, or even days, which are important for predicting the wind farm production, are difficult to quantify from LES but are relatively easy to obtain from field measurements. In the next section, we will examine the wind speed variations in turbine wakes using the field measured data. In Sections 3.2 and 3.3 we will probe into the predictive ability

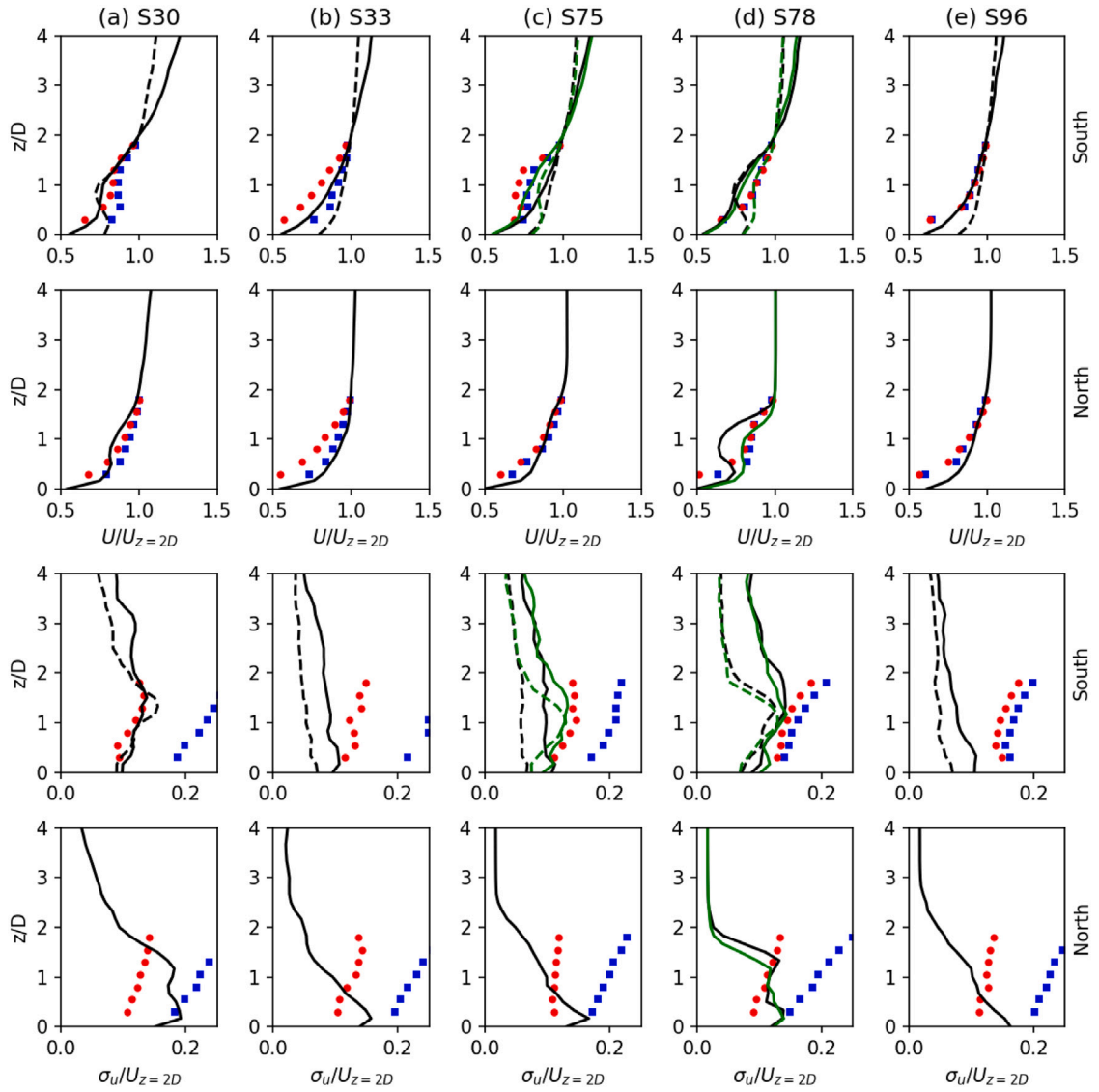

Fig. 13. Comparison of the vertical profiles of the computed time-averaged downwind velocity (top) and the standard deviations of downwind velocity fluctuations (bottom) between LES predictions (black solid lines) and SODAR measurements (red circles, blue squares) at different SODAR locations. The measured data (red circles and blue squares) are post-processed using Eq. (4). The red circles are post-processed using all three constraints. The blue squares, on the other hand, are post-processed using constraints C_1 and C_2. Green lines in (c) and (d) denote the LES-predicted vertical profiles located $1.8D$ east of S75 and $0.5D$ east of S78 (S75 and S78 locations can be found in Fig. 1), respectively.

of LES for a short time period by comparing the computed results with measurements.

3.1. Wind speed distribution in turbine wakes

The Weibull distribution is often employed in the literature for characterizing wind distribution as we discussed in the introduction section. In this section, we examine whether the Weibull distribution is still valid for the wind speed in turbine wakes. At the S30 and S75 SODAR locations, velocity deficits are observed for wind from the south direction. The wind speed PDFs in turbine wakes are examined in Fig. 7 with the corresponding wind profiles shown in the far left column, where the top tip and bottom tip of the turbine are indicated by red dashed lines. It is seen from the velocity profiles that the velocity deficits are higher during the night, which is reasonable since the stable stratification condition during nights slow down the wake recovery. The wake at S75 is observed to be less significant than that at S30, which is due to the fact that the closest upwind turbine is not located directly upwind. It should be also noted that S75 is located at the top of a hill after an abrupt change of terrain elevations, while S30 is located deep in the wind farm where terrain topography changes are small. From the PDF plots shown in Fig. 7, we can see that the Weibull distribution fits very well with the measured data except for the PDF of the wind speed measured at $S75$ at vertical locations above the hub height during nights. For all PDFs, it is observed that the shape factor is lower during nights, which indicates higher variations of the wind speed.

Before examining the shape factors of the Weibull distribution in turbine wakes, we plot the contours of shape factors as a function of wind direction and distance from the ground in Fig. 8. It is seen that the shape factor remains fairly constant in the vertical direction, but changes with wind directions for all the SODAR locations. The values of k during nights are observed to be different from those during days, which become even higher and lower during nights for the wind direction with higher and lower k values, respectively. It is also observed that the k values can be significantly higher than the recommended value [72], which does not consider the terrain and turbine wake effects. To investigate how the values of the shape factor k depend on the wind speed, we average k in the vertical location and plot the vertically averaged $\langle k \rangle$ as a function of the vertically averaged

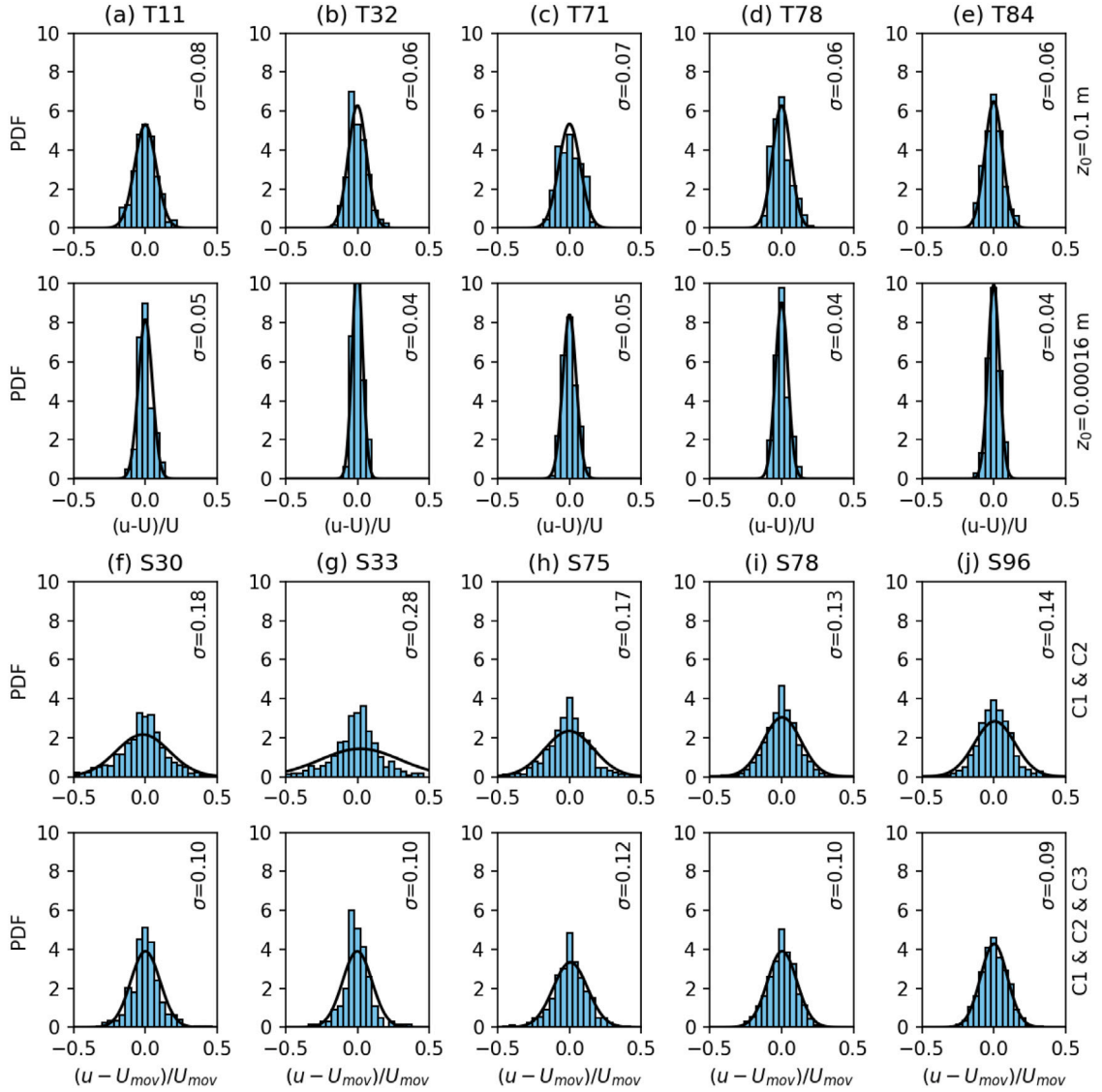

Fig. 14. Comparison of the PDF of wind speed fluctuations between (a) and (b) LES and (c) and (d) SODAR measurements for the cases with wind from the south direction. The PDFs of measured data shown in (c) and (d) are post-processed using Eq. (4) with the constraints C_1 and C_2, and with all three constraints, respectively. The solid lines are the fitted Gaussian distribution.

wind speed $\langle U \rangle$ in Fig. 9. It is seen that the shape factor approximately increases as a function of the wind speed. The red points show the shape factors for measurements in turbine wakes. It is seen that the values of vertically averaged k for measurements in wakes are lower than those out of wakes, which should be considered when designing a wind farm. In summary, the Weibull distribution in general can be considered valid in turbine wakes based on the measured data, but with a shape factor lower than that in the ambient atmosphere.

The wind field in the atmosphere is characterized by varying wind speed, wind direction, and thermal stratification conditions across all relevant times scales (i.e. from hours to years). Characterizing the wind field using LES for different atmospheric conditions and different time scales requires a huge amount of computational resources, which are beyond the practical time frame for designing a wind farm. Usually idealized LES over a short period of time under statistically steady inflow conditions is feasible for informing wind farm design, as we do in this work. In the following two sections we aim to examine the predictive usefulness of such idealized LES by comparing the LES results with SCADA (Supervisory Control and Data Acquisition) and SODAR measurements.

3.2. Comparison of simulation results with SCADA data

In this section we compare the wind speed computed using LES with that measured by SCADA. The SCADA wind speeds are averaged every 10 min. To facilitate the comparisons, the simulated wind speeds are averaged over a circular disk with the same radius and orientation as the turbine rotor located one rotor diameter upwind. The SCADA data in the range of $[175°, 185°]$ are employed for comparison while the wind in the simulation is exactly from the south direction. There are 100 turbines in the wind farm, which makes the comparison per turbine difficult and not helpful for analyzing the spatial wind speed variation. We thus divide the turbines into 21 groups (as shown in Fig. 1) and investigate the wind speed variations among groups and within each group.

We first compare the group-averaged wind speed between LES and SCADA results in Fig. 10. It is seen that LES predicts the overall pattern of the downwind variation of wind speed for both wind directions, which is caused by the terrain elevation as well as turbine wakes. However, there are some differences between the LES predictions and measurements especially near the inlet of the computational domain, i.e. groups G1-2 and groups G18-21 as shown in Fig. 10 for wind

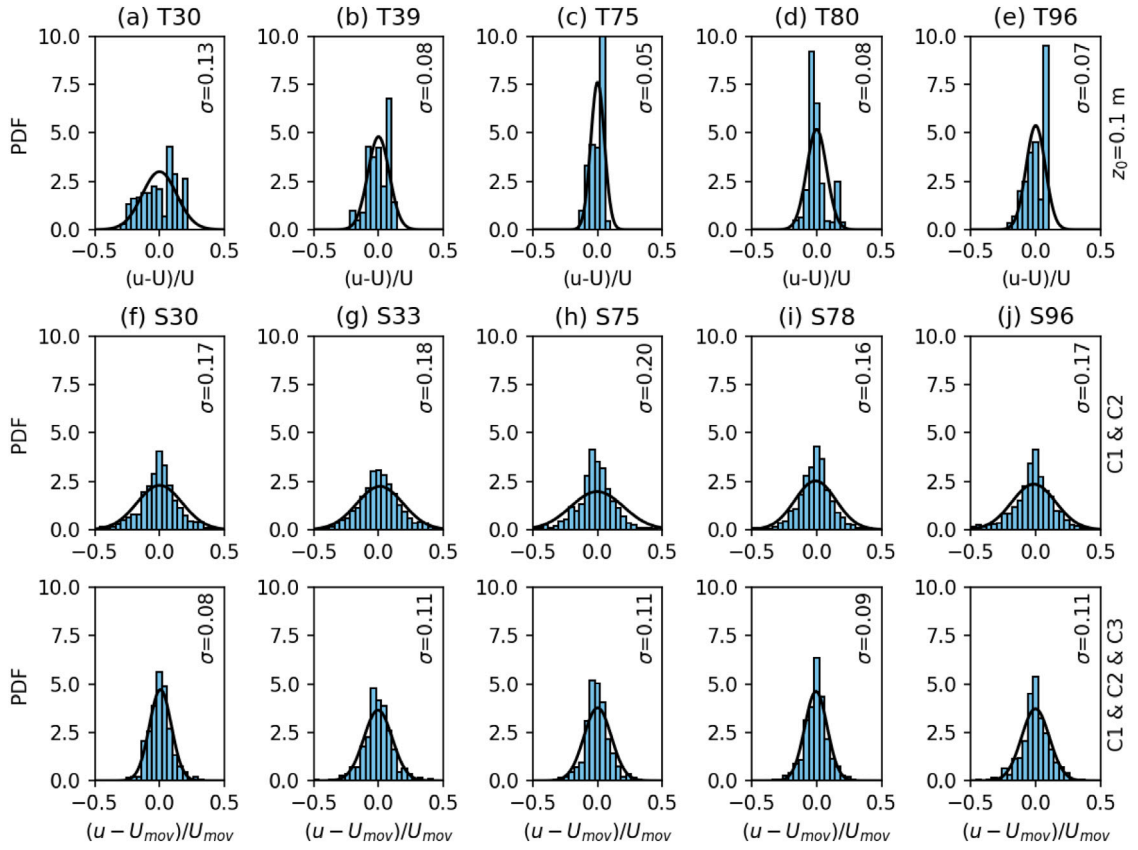

Fig. 15. Comparison of the PDF of wind speed fluctuations between (a) LES and (b) and (c) SODAR measurements for the case with wind from the north direction. The PDFs of measured data shown in (b) and (c) are post-processed using Eq. (4) with the constraints C_1 and C_2, and with all three constraints, respectively. The solid lines are the fitted Gaussian distribution.

from the south and north directions, respectively. These differences are probably caused by the fact that the inflow generated from a precursory simulation of flat terrain does not take into account the effects of the actual terrain far upwind of the wind farm. For the case with wind blowing from the south, the differences between results from different roughness lengths are minor until group G14 especially for group G18, for which the velocity predicted by the simulation with $z_0 = 0.00016$ m is significantly lower than that from $z_0 = 0.1$ m case. For the case with wind from the north direction, LES fails to predict the velocity increase from group 6 to 5 and 4, which is probably caused by the relatively coarse grid employed in LES. In Figs. 11 and 12 we show the wind speed variation within each group for all the cases. Overall the wind speed variation within each group is well predicted by LES with some discrepancies observed in several groups, e.g. G9 and G11 for wind from the south direction, and G13 and G17 for wind from the north direction.

3.3. Comparison of simulation results with SODAR data

In this section, we compare the LES results with SODAR measurements. However, we do not aim to directly compare the computed results with a specific period of measured data. Instead we intend to explore the predictive usefulness of a LES under idealized conditions over time scales much longer than those LES is typically used for. The measured wind velocity and turbulence intensity employed for comparison are calculated by averaging the corresponding moving-average values under certain constraints as follows:

$$\langle f(z)\rangle = \frac{1}{N}\sum_{i=0}^{N}\left(\bar{f}_{mov}(t_i,z)\big|_{C_1\ \&\ C_2\ \&\ C_3}\right), \tag{4}$$

where $f(z)$ is the quantity of concern, $\bar{f}_{mov}(t_i,z)$ is the moving averaged value (which can be the mean wind speed or turbulence intensity normalized using the corresponding moving-averaged wind speed), N is the number of all samples that satisfy the three constraints, i.e., C_1 : $\bar{U}_{mov}(t_i,z_h) \in [U_1,U_2]$, C_2 : $\bar{\phi}(t_i,2D) \in [\phi_1,\phi_2]$ and C_3 : $\sigma_{u,mov}(t_i,2D) < \sigma_{crit}$. The first constraint ensures that the turbine operates in regime 2, i.e. the same as in the simulations, for comparison with the simulation results. The second constraint constrains the wind direction. The third constraint assures that the standard deviations due to low frequency (~ hours) wind speed variations are not accounted for in the computation of turbulence intensity as they are beyond the predictive ability of an idealized LES as defined above. In this work U_1 and U_2 are set as the cut-in and rated wind speed of the turbine, $\phi_1 = 175°$ and $\phi_2 = 185°$, and $\sigma_{crit}/U = 0.18$ (where U is mean downwind velocity at the same location), respectively.

In Fig. 13 we compare the simulated (black lines) mean downwind velocity and turbulence intensity with the SODAR measurements for all the cases, which are conditionally-averaged using different constraints. Specifically, the red symbols are the measurements conditionally averaged using all the constraints (equation (4)) while the blue symbols are the measured data conditionally averaged using only constraints C_1 and C_2 (i.e. allowing for contributions from low frequency variations in the wind farm and the atmosphere). It is seen that overall good agreement is obtained between the LES predictions and measurements when the measured data are conditionally averaged using all the constraints. On the other hand, discrepancies are observed when only constraints C_1 and C_2 are employed especially for the turbulence intensity. A good agreement between the computed turbulence intensity and that from the measured data conditionally averaged using all constraints is also obtained. Without employing the third constraint C_3, the shapes of

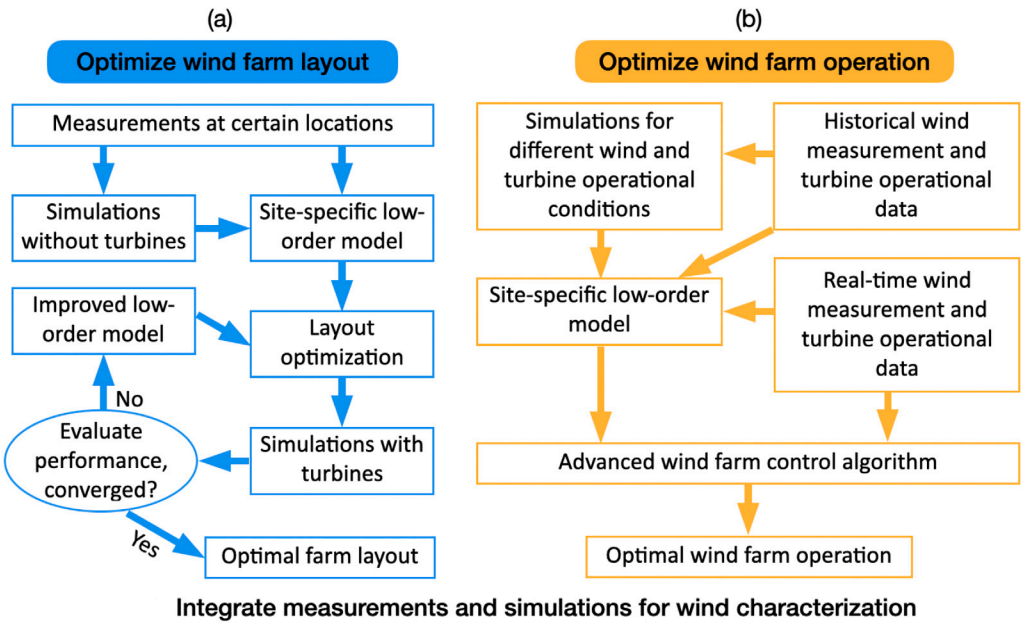

Fig. 16. A schematic for a potential solution for integrating measurements and simulations for (a) wind farm layout optimization and (b) wind farm operation optimization.

the vertical profile of σ_u are very different, and the magnitudes of the measured σ_u are approximately two times greater than the computed results. It is noticed that at the S75 location a wake profile is observed in the measurement when wind blows from the south, which, however, does not exist in the simulation. This discrepancy is probably caused by the misalignment of the rotor with the wind direction, which is not considered in the simulation. To compare the LES-predicted wake profiles with measurements, we added the LES-predicted vertical profiles located $1.8D$ east from S75 to Fig. 13(c). It is seen that the vertical profile of U and σ_u are in good agreement with the measurements at this location. At S78 location, the velocity deficit from LES is observed being larger than that from the measurements. It is possibly because of the misalignment of rotor with the downwind direction, such that what SODAR measured represents the quantities on the boundary of the wake instead of center of the wake. In order to verify this conjecture to some extent, we plot the vertical profiles located $0.5D$ east of the S78 location in Fig. 13(d). It is seen that vertical profiles of U and σ_u agree better with measurements at this new location.

The PDF profiles of wind speed fluctuations predicted using LES are compared with measurements in Figs. 14 and 15 for wind blowing from the south and north directions, respectively. The PDF profiles from the LES predictions are computed using the time series of the downwind velocity averaged over a circular disk of the same radius as the rotor located at one rotor diameter upwind of the turbine. The PDF profiles from the SODAR measurements are computed using the vertically averaged (from $z = 45$ m to $z = 145$) wind speed for wind directions $180° \pm 5°$ and $0° \pm 5°$ for wind from the south and the north, respectively. The velocity fluctuations for computing the PDF from SODAR measurements are obtained by post-processing the vertically averaged wind speed using the moving average and conditionally-averaged procedure (i.e., Eq. (4)). It is seen that the computed PDF profiles (the first row of Fig. 14) agree better with the measured values (the fourth row of Fig. 14), which are post-processed using all three constraints. It is also noticed that both computed and measured PDF distributions post-processed using all three constraints can be approximated reasonably well using the Gaussian distribution. The measured PDF distributions shown in third column of Fig. 14(c), which are post-processed without using the constraint C_3, on the other hand, deviate significantly from the Gaussian distribution. The values of the standard deviations are also observed to be much larger. For the case with wind from the north direction, similar trend is observed in Fig. 15.

3.4. A potential solution for integrating measurements and simulations

In this section, we attempt to discuss a potential solution for integrating measurements and simulations for wind field characterization in large-scale wind farms or potential sites. We consider two scenarios, one for wind farm layout optimization and the other for the optimization of wind farm operation. A schematic for this solution is shown in Fig. 16. Because of its high computational cost, it is not feasible to directly employ LES for the design and operation of wind farms. The key element of the proposed solution is the use of site-specific low-order wind farm models.

In the scenario of wind farm layout optimization, the wind field measurement campaign is firstly carried out at certain locations as shown in Fig. 16(a). Using the measured wind speed as inputs, simulations without wind turbines are then carried out for different wind conditions (e.g. different wind directions, wind speeds, thermal stratification conditions and etc.). With the simulation results, site-specific low-order wind farm models can then be developed using the measured and simulation data either based on existing models or totally driven by the data using the machine learning method [73–75]. This site-specific low-order models are then combined with an optimization method to find the optimal turbine locations. With the obtained turbine locations, simulations with turbines are then carried out to assess the performance of the layout and to improve the low-order models to better account for turbine wake effects. Iterations are needed here until the convergence of the wind farm performance is achieved.

In the scenario of optimizing wind farm operation, simulations for different wind and turbine operational conditions are first carried out based on the historical wind measurements and turbine operational data as shown in Fig. 16(b). With the measured and simulation data, site-specific low-order models can then be developed based on existing models or using a data-driven approach. The developed low-order models are then combined with the advanced wind farm control algorithm for optimal wind farm operations using the real-time wind speed measurement data and the turbine operational data as inputs.

It should be noted that this is just a blueprint for the integration of measurements and simulations for wind field characterization. A lot of

work still needs to be done to realize this solution especially for the development low-order wind farm models, for instance, how to incorporate the effects of complex topography in low-order models using the data from measurements and high-fidelity simulations [46,49,76,77], and how to take into account the effect of inflow turbulence, which can significantly affects turbine wakes and wind farm performance as shown in this work and in the literature [78,79]. This can be explored either by calibrating the parameters of the existing models, introducing more physics to the existing models, or following a data-driven approach. Moreover, further development of wake models may also be needed for non-conventional wind farm configurations, e.g. turbine staggering in the vertical direction [80,81].

4. Conclusions

In this work we presented the field measurements and LES results obtained with the turbines parameterized as actuator lines of a utility-scale wind farm of 100 wind turbines to explore the possibility of using LES and field measurements to characterize wind fields in utility-scale wind farms across a range of time scales. In the field measurements the wind speed data were collected at each turbine via the SCADA system and at several locations within the wind farm using SODAR.

Using the SODAR-collected data the distributions of wind speed and wind direction are examined at the five locations. It is found that both wind direction and wind speed distributions can be well approximated using the Weibull distribution. For certain wind directions wake profiles were observed at several SODAR locations. Special attention was paid on the measured wake data. It is observed that the Weibull distribution is still a reasonable approximation of the wind speed in the turbine wake with some discrepancies observed for one case at locations far away ($z = 130, 180$ m) from the ground. The shape factor of the Weibull distribution was examined and shown to increase in general with the mean velocity. One interesting observation is that the values of shape factors corresponding to turbine wakes are lower than others without turbine wake effects. This finding implies a high probability of having velocities significantly higher or lower than the expected value in turbine wakes.

The LES predictions are compared with both SCADA data and SODAR data. For the comparison with SCADA data, the LES is shown to predict both the variation of group-averaged power and the variation of power within each group, which is consistent with what we have also found in our previous work for a wind farm in complex terrain. Some discrepancies are also observed, which might be caused by unresolved terrain topography or the inflow not fully taking into account the effects of terrain far upwind of the wind turbines. The LES computed results are compared with SODAR for both mean velocities and downwind turbulence intensities. In the simulation both wind speed and wind direction are statistically stationary. This assumption, however, is not fulfilled in the SODAR measurements, which have been obtained over different seasons and across time scales when significant variations of wind speed and direction occur. For that, and to avoid computing contributions of low frequency (hourly) wind speed variation in the measured turbulence intensity, a moving average procedure with constraints on the standard deviation of wind speed at $z = 200$ m was developed and implemented to process the SODAR measurements. It is found that the vertical profiles of both wind speed and downwind turbulence intensity agree well with the conditionally-averaged SODAR measurements. The computed PDF profiles of velocity fluctuations are also compared with SODAR data. A good agreement between the simulation results and the measured data is observed when the above mentioned constraint is enforced during the post-processing of the measured data.

In summary, the good agreement between LES prediction and measurements suggests that an idealized LES over a short time interval can reasonably represent the mean wind speed and turbulence intensities ensemble-averaged over many short time intervals when large-scale wind speed variations are absent. The measurements, on the other hand, can provide statistics over a long time interval, such as the PDFs of wind speeds and wind directions, which cannot be easily obtained using high-fidelity simulations. Overall, the present work shows the possibility of integrating high-fidelity simulations and measurements for characterizing wind resources in utility-scale wind farms with a potential solution for integrating measurements and high-fidelity simulations discussed in Section 3.4. More work, such as considering the effects of complex terrain, thermal stratification and ocean waves, and LES under varying wind conditions, needs to be carried out to realize the possibility of integrating field measurements and LES for wind resource assessment in the design of very large land-based or offshore wind farms.

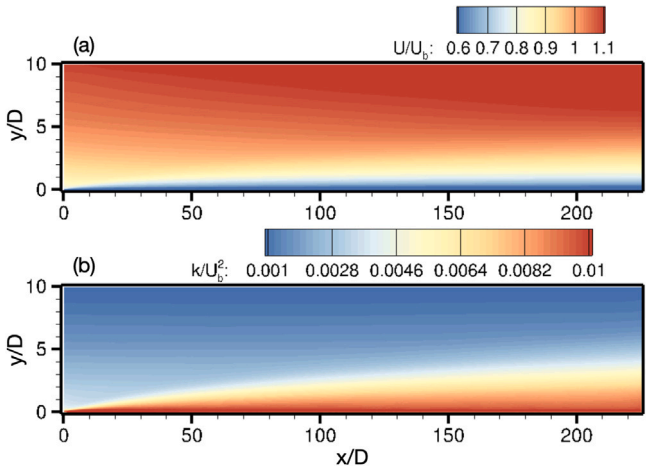

Fig. 17. Streamwise development of (a) the time-averaged downwind velocity U and (b) the turbulence kinetic energy k in the simulation for generating inflow for the wind farm cases with roughness length of 0.1 m.

CRediT authorship contribution statement

Xiaolei Yang: Conceptualization, Methodology, Software, Validation, Writing - original draft, Writing - review & editing, Visualization. **Christopher Milliren:** Field data collection. **Matt Kistner:** Field data collection. **Christopher Hogg:** Field data collection. **Jeff Marr:** Field data collection. **Lian Shen:** Resources, Writing - review & editing. **Fotis Sotiropoulos:** Conceptualization, Methodology, Resources, Writing - review & editing, Supervision, Project administration, Funding acquisition.

Declaration of competing interest

The authors declare that they have no known competing financial interests or personal relationships that could have appeared to influence the work reported in this paper.

Acknowledgments

This work was supported by Xcel Energy, United States through the Renewable Development Fund (RD4-13 and HE4-3). Computational resources were provided by the University of Minnesota Supercomputing Institute, United States, the Institute for Advanced Computational Science at the Stony Brook University, United States, and TH-2 supercomputer at the National Supercomputer Center, Guangzhou, China.

Appendix

For the wind farm case with roughness length of 0.1 m, the inflow is generated by applying the inflow from the precursory simulation with roughness length of 0.00016 m to the simulation with inlet–outlet boundary condition in the downwind direction, roughness length of 0.1 m and the same parameters for other computational setup. The length of the computational domain for this simulation is $225D$. The velocity field on the slice located at $220D$ from the inlet is employed as the inflow for the wind farm simulation. In this appendix, we show the downwind variations of the time-averaged downwind velocity U and the turbulence kinetic energy k in this simulation. As seen in Fig. 17, at $220D$ from the inlet, the flow is very close to the fully developed state.

References

[1] (IEA) IEA. World energy outlook 2018. Tech. rep., IEA; 2018, URL www.iea.org/weo2018/. [Last accessed June 2020].

[2] DNV G. Energy transition outlook 2018: A global and regional forecast of the energy transition to 2050. 2018, URL https://eto.dnvgl.com/2018/. [Last accessed June 2020].

[3] BNEF. New energy outlook 2019. 2019, URL https://about.bnef.com/new-energy-outlook/. [Last accessed June 2020].

[4] Stevens RJ, Meneveau C. Flow structure and turbulence in wind farms. Annu Rev Fluid Mech 2017;49:311–39.

[5] Veers P, Dykes K, Lantz E, Barth S, Bottasso CL, Carlson O, et al. Grand challenges in the science of wind energy. Science 2019;366(6464):eaau2027.

[6] Mosetti G, Poloni C, Diviacco B. Optimization of wind turbine positioning in large windfarms by means of a genetic algorithm. J Wind Eng Ind Aerodyn 1994;51(1):105–16.

[7] Kusiak A, Song Z. Design of wind farm layout for maximum wind energy capture. Renew Energy 2010;35(3):685–94.

[8] Morales JM, Minguez R, Conejo AJ. A methodology to generate statistically dependent wind speed scenarios. Appl Energy 2010;87(3):843–55.

[9] Yip CMA, Gunturu UB, Stenchikov GL. Wind resource characterization in the Arabian Peninsula. Appl Energy 2016;164:826–36.

[10] Kirchner-Bossi N, Prieto L, García-Herrera R, Carro-Calvo L, Salcedo-Sanz S. Multi-decadal variability in a centennial reconstruction of daily wind. Appl Energy 2013;105:30–46.

[11] Langodan S, Viswanadhapalli Y, Dasari HP, Knio O, Hoteit I. A high-resolution assessment of wind and wave energy potentials in the Red sea. Appl Energy 2016;181:244–55.

[12] Zhang J, Draxl C, Hopson T, Delle Monache L, Vanvyve E, Hodge B-M. Comparison of numerical weather prediction based deterministic and probabilistic wind resource assessment methods. Appl Energy 2015;156:528–41.

[13] Landberg L, Myllerup L, Rathmann O, Petersen EL, Jørgensen BH, Badger J, et al. Wind resource estimation—an overview. Wind Energy 2003;6(3):261–71.

[14] Ayotte KW. Computational modelling for wind energy assessment. J Wind Eng Ind Aerodyn 2008;96(10–11):1571–90.

[15] Sempreviva AM, Barthelmie RJ, Pryor S. Review of methodologies for offshore wind resource assessment in European seas. Surv Geophys 2008;29(6):471–97.

[16] Probst O, Cárdenas D. State of the art and trends in wind resource assessment. Energies 2010;3(6):1087–141.

[17] Christiansen MB, Koch W, Horstmann J, Hasager CB, Nielsen M. Wind resource assessment from C-band SAR. Remote Sens Environ 2006;105(1):68–81.

[18] He G, Kammen DM. Where, when and how much wind is available? A provincial-scale wind resource assessment for China. Energy Policy 2014;74:116–22.

[19] Doubrawa P, Barthelmie RJ, Pryor SC, Hasager CB, Badger M, Karagali I. Satellite winds as a tool for offshore wind resource assessment: The Great Lakes Wind Atlas. Remote Sens Environ 2015;168:349–59.

[20] Acker TL, Williams SK, Duque EP, Brummels G, Buechler J. Wind resource assessment in the state of Arizona: Inventory, capacity factor, and cost. Renew Energy 2007;32(9):1453–66.

[21] Jafari S, Sommer T, Chokani N, Abhari RS. Wind resource assessment using a mesoscale model: the effect of horizontal resolution. In: Turbo expo: power for land, sea, and air, vol. 44724. American Society of Mechanical Engineers; 2012, p. 987–95.

[22] Al-Yahyai S, Charabi Y, Gastli A. Review of the use of numerical weather prediction (NWP) models for wind energy assessment. Renew Sustain Energy Rev 2010;14(9):3192–8.

[23] Carvalho D, Rocha A, Santos CS, Pereira R. Wind resource modelling in complex terrain using different mesoscale–microscale coupling techniques. Appl Energy 2013;108:493–504.

[24] Gasset N, Landry M, Gagnon Y. A comparison of wind flow models for wind resource assessment in wind energy applications. Energies 2012;5(11):4288–322.

[25] Defforge CL, Carissimo B, Bocquet M, Bresson R, Armand P. Improving CFD atmospheric simulations at local scale for wind resource assessment using the iterative ensemble Kalman smoother. J Wind Eng Ind Aerodyn 2019;189:243–57.

[26] Veronesi F, Grassi S, Raubal M. Statistical learning approach for wind resource assessment. Renew Sustain Energy Rev 2016;56:836–50.

[27] Fuglsang P, Antoniou I, Dahl K, Madsen H. Wind tunnel tests of the FFA-W3-241, FFA-W3-201 and NACA-63-430 airfoils. Denmark Risø National Laboratory; 1998.

[28] Aukitino T, Khan MG, Ahmed M. Wind energy resource assessment for Kiribati with a comparison of different methods of determining Weibull parameters. Energy Convers Manage 2017;151:641–60.

[29] Palma J, Castro FA, Ribeiro LF, Rodrigues A, Pinto A. Linear and nonlinear models in wind resource assessment and wind turbine micro-siting in complex terrain. J Wind Eng Ind Aerodyn 2008;96(12):2308–26.

[30] Jimenez B, Durante F, Lange B, Kreutzer T, Tambke J. Offshore wind resource assessment with WAsP and MM5: comparative study for the German Bight. Wind Energy 2007;10(2):121–34.

[31] Yan B, Li Q. Coupled on-site measurement/CFD based approach for high-resolution wind resource assessment over complex terrains. Energy Convers Manage 2016;117:351–66.

[32] Tang X-Y, Zhao S, Fan B, Peinke J, Stoevesandt B. Micro-scale wind resource assessment in complex terrain based on CFD coupled measurement from multiple masts. Appl Energy 2019;238:806–15.

[33] Song M, Chen K, He Z, Zhang X. Wind resource assessment on complex terrain based on observations of a single anemometer. J Wind Eng Ind Aerodyn 2014;125:22–9.

[34] Simões T, Estanqueiro A. A new methodology for urban wind resource assessment. Renew Energy 2016;89:598–605.

[35] Bechrakis D, Deane J, McKeogh E. Wind resource assessment of an area using short term data correlated to a long term data set. Sol Energy 2004;76(6):725–32.

[36] Weekes S, Tomlin A. Data efficient measure-correlate-predict approaches to wind resource assessment for small-scale wind energy. Renew Energy 2014;63:162–71.

[37] Vanvyve E, Delle Monache L, Monaghan AJ, Pinto JO. Wind resource estimates with an analog ensemble approach. Renew Energy 2015;74:761–73.

[38] Sharma PK, Warudkar V, Ahmed S. Application of LiDAR and measure correlate predict method in offshore wind resource assessments. J Cleaner Prod 2019;215:534–43.

[39] Lackner MA, Rogers AL, Manwell JF. Uncertainty analysis in MCP-based wind resource assessment and energy production estimation. J Sol Energy Eng 2008;130(3).

[40] Miguel JV, Fadigas EA, Sauer IL. The influence of the wind measurement campaign duration on a measure-correlate-predict (MCP)-based wind resource assessment. Energies 2019;12(19):3606.

[41] Wan C, Wang J, Yang G, Li X, Zhang X. Optimal micro-siting of wind turbines by genetic algorithms based on improved wind and turbine models. In: Proceedings of the 48th IEEE conference on decision and control (CDC) held jointly with 2009 28th Chinese control conference. IEEE; 2009, p. 5092–6.

[42] Thomsen K, Sørensen P. Fatigue loads for wind turbines operating in wakes. J Wind Eng Ind Aerodyn 1999;80(1–2):121–36.

[43] Troldborg N, Sorensen JN, Mikkelsen R. Numerical simulations of wake characteristics of a wind turbine in uniform inflow. Wind Energy 2010;13(1):86–99.

[44] Porté-Agel F, Wu Y-T, Lu H, Conzemius RJ. Large-eddy simulation of atmospheric boundary layer flow through wind turbines and wind farms. J Wind Eng Ind Aerodyn 2011;99(4):154–68.

[45] Yang X, Sotiropoulos F, Conzemius RJ, Wachtler JN, Strong MB. Large-eddy simulation of turbulent flow past wind turbines/farms: the virtual wind simulator (VWiS). Wind Energy 2015;18(12):2025–45.

[46] Yang X, Pakula M, Sotiropoulos F. Large-eddy simulation of a utility-scale wind farm in complex terrain. Appl Energy 2018;229:767–77.

[47] Yang X, Sotiropoulos F. A new class of actuator surface models for wind turbines. Wind Energy 2018;21(5):285–302.

[48] Germano M, Piomelli U, Moin P, Cabot WH. A dynamic subgrid-scale eddy viscosity model. Phys Fluids A 1991;3(7):1760–5, (1989–1993).

[49] Yang X, Howard KB, Guala M, Sotiropoulos F. Effects of a three-dimensional hill on the wake characteristics of a model wind turbine. Phys Fluids 2015;27(2):025103.

[50] Yang X, Hong J, Barone M, Sotiropoulos F. Coherent dynamics in the rotor tip shear layer of utility-scale wind turbines. J Fluid Mech 2016;804:90–115.

[51] Yang X, Boomsma A, Barone M, Sotiropoulos F. Wind turbine wake interactions at field scale: An LES study of the SWiFT facility. In: J Phys Conf Ser. 524, (1):IOP Publishing; 2014, 012139.

[52] Yang X, Sotiropoulos F. Wake characteristics of a utility-scale wind turbine under coherent inflow structures and different operating conditions. Phys Rev Fluids 2019;4(2):024604.

[53] Foti D, Yang X, Shen L, Sotiropoulos F. Effect of wind turbine nacelle on turbine wake dynamics in large wind farms. J Fluid Mech 2019;869:1–26.

[54] Foti D, Yang X, Sotiropoulos F. Similarity of wake meandering for different wind turbine designs for different scales. J Fluid Mech 2018;842:5–25.

[55] Yang X, Zhang X, Li Z, He G-W. A smoothing technique for discrete delta functions with application to immersed boundary method in moving boundary simulations. J Comput Phys 2009;228(20):7821–36.

[56] Shen WZ, Zhang JH, Sørensen JN. The actuator surface model: a new Navier–Stokes based model for rotor computations. J Solar Energy Eng 2009;131(1):011002.
[57] Massie L, Ouro P, Stoesser T, Luo Q. An actuator surface model to simulate vertical axis turbines. Energies 2019;12(24):4741.
[58] Wu J. Wind-stress coefficients over sea surface from breeze to hurricane. J Geophys Res Oceans 1982;87(C12):9704–6.
[59] Hansen FV. Surface roughness lengths. Tech. rep, Army Research Lab White Sands Missile Range NM; 1993.
[60] Wu Y-T, Porté-Agel F. Atmospheric turbulence effects on wind-turbine wakes: An LES study. Energies 2012;5(12):5340–62.
[61] Chamorro LP, Arndt R, Sotiropoulos F. Reynolds number dependence of turbulence statistics in the wake of wind turbines. Wind Energy 2012;15(5):733–42.
[62] Hansen MO. Aerodynamics of wind turbines. Routledge; 2015.
[63] Iungo GV, Wu Y-T, Porté-Agel F. Field measurements of wind turbine wakes with LiDARs. J Atmos Ocean Technol 2013;30(2):274–87.
[64] Hong J, Toloui M, Chamorro LP, Guala M, Howard K, Riley S, Tucker J, Sotiropoulos F. Natural snowfall reveals large-scale flow structures in the wake of a 2.5-MW wind turbine. Nature Commun 2014;5:4216.
[65] Chamorro LP, Lee S-J, Olsen D, Milliren C, Marr J, Arndt R, et al. Turbulence effects on a full-scale 2.5 MW horizontal-axis wind turbine under neutrally stratified conditions. Wind Energy 2015;18(2):339–49.
[66] Howard KB, Guala M. Upwind preview to a horizontal axis wind turbine: a wind tunnel and field-scale study. Wind Energy 2016;19(8):1371–89.
[67] El-Asha S, Zhan L, Iungo GV. Quantification of power losses due to wind turbine wake interactions through SCADA, meteorological and wind LiDAR data. Wind Energy 2017;20(11):1823–39.
[68] Heisel M, Hong J, Guala M. The spectral signature of wind turbine wake meandering: A wind tunnel and field-scale study. Wind Energy 2018;21(9):715–31.
[69] Churchfield M, Lee S, Moriarty P, Martinez L, Leonardi S, Vijayakumar G, et al. A large-eddy simulation of wind-plant aerodynamics. In: 50th AIAA aerospace sciences meeting including the new horizons forum and aerospace exposition, 2012. p. AIAA–537.
[70] Stevens RJ, Gayme DF, Meneveau C. Large eddy simulation studies of the effects of alignment and wind farm length. J Renew Sustain Energy 2014;6(2):023105.
[71] Yang D, Meneveau C, Shen L. Large-eddy simulation of offshore wind farm. Phys Fluids 2014;26(2):025101.
[72] Burton T, Sharpe D, Jenkins N, Bossanyi E. Wind energy handbook, vol. 2. Wiley Online Library; 2001.
[73] Bishop CM. Pattern recognition and machine learning. Springer; 2006.
[74] Duraisamy K, Iaccarino G, Xiao H. Turbulence modeling in the age of data. Annu Rev Fluid Mech 2019;51:357–77.
[75] Brunton SL, Noack BR, Koumoutsakos P. Machine learning for fluid mechanics. Annu Rev Fluid Mech 2020;52:477–508.
[76] Feng J, Shen WZ, Li Y. An optimization framework for wind farm design in complex terrain. Appl Sci 2018;8(11):2053.
[77] Liu L, Stevens RJ. Effects of two-dimensional steep hills on the performance of wind turbines and wind farms. Bound Layer Meterol 2020;176:251–69.
[78] Wu Y-T, Lin C-Y, Chang T-J. Effects of inflow turbulence intensity and turbine arrangements on the power generation efficiency of large wind farms. Wind Energy 2020;23:1640–55.
[79] Li Z, Yang X. Evaluation of actuator disk model relative to actuator surface model for predicting utility-scale wind turbine wakes. Energies 2020;13(14):3574.
[80] Wu Y-T, Liao T-L, Chen C-K, Lin C-Y, Chen P-W. Power output efficiency in large wind farms with different hub heights and configurations. Renew Energy 2019;132:941–9.
[81] Zhang M, Arendshorst MG, Stevens RJ. Large eddy simulations of the effect of vertical staggering in large wind farms. Wind Energy 2019;22(2):189–204.